A hybrid mathematical model for self-organizing cell migration in the zebrafish lateral line

Journal of Mathematical Biology manuscript No.
(will be inserted by the editor)

A hybrid mathematical model for self-organizing cell migration in the zebrafish lateral line

E. Di Costanzo · R. Natalini · L. Preziosi

Received: date / Accepted: date

Abstract In this paper we propose a *discrete in continuous* mathematical model for the morphogenesis of the posterior lateral line system in zebrafish. Our model follows closely the results obtained in recent biological experiments. We rely on a hybrid description: discrete for the cellular level and continuous for the molecular level. We prove the existence of steady solutions consistent with the formation of particular biological structure, the neuromasts. Dynamical numerical simulations are performed to show the behavior of the model and its qualitative and quantitative accuracy to describe the evolution of the cell aggregate.

Keywords cell migration · self-organization · embryogenesis · zebrafish · neuromasts formation · cellular signaling

Mathematics Subject Classification (2000) 92B05 · 92C17 · 92C15

E. Di Costanzo
Dipartimento di Scienze di Base e Applicate per l'Ingegneria – Sezione di Matematica,
Sapienza University of Rome,
Via A. Scarpa 16, I-00161 Rome, Italy.
E-mail: ezio.dicostanzo@sbai.uniroma1.it

R. Natalini (corresponding author)
Istituto per le Applicazioni del Calcolo "Mauro Picone",
Consiglio Nazionale delle Ricerche,
Via dei Taurini 19, I-00185 Roma, Italy
Tel.: +39-0649270961
Fax: +39-0672594699
E-mail: roberto.natalini@cnr.it

L. Preziosi
Department of Mathematical Sciences,
Politecnico di Torino,
Corso Duca degli Abruzzi 24, I-10129 Turin, Italy
E-mail: luigi.preziosi@polito.it

1 Introduction

The *lateral line* is a sensory system, which is present in fish and amphibians, that is used to detect movement and vibration in the surrounding water and is involved in a large variety of behaviors, from prey detection to predator avoidance, school swimming and sexual courtship. It extends from the head to the tail along each flank of the fish, and it is formed by a set of sensory organs, the *neuromasts*, arranged on the body surface in specific patterns. The neuromasts, located between the ear and the eye, form the so-called anterior lateral line system (ALL), while neuromasts on the body and tail form the *posterior lateral line* system (PLL) (Ghysen and Chaudière, 2004; Coombs and Netten, 2005).

In this paper we propose and analyze a mathematical model for the morphogenesis of the *zebrafish* (*Danio rerio*) PLL. The development of this sensory organ represents a subject of general importance, as a paradigm to understand the growth, regeneration, and self-organization of other organ systems during development and disease (Chitnis et al, 2012). Recent studies (Haas and Gilmour, 2006; Nechiporuk and Raible, 2008; Lecaudey et al, 2008) (see also Haddon et al, 1998; Itoh and Chitnis, 2001; Draper et al, 2001; Ghysen and Chaudière, 2004; Li et al, 2004; Matsuda and Chitnis, 2010; Sarrazin et al, 2010; Mizoguchi et al, 2011; Sweet et al, 2011) have investigated migration and self-organization in the zebrafish lateral line system, where a complex system of receptor activation drives embryonic cells, rather than a guidance determined by birth. However, the complete mechanism for cells arranging and organization is still relatively poorly understood (Lecaudey et al, 2008).

Loosely speaking, lateral line formation consists in a group of mesenchymal cells (called primordium) that migrate driven by a haptotactic signal. In a second phase, a process of differentiation in the rear of the migrating group induces a mesenchymal-epithelial transition (in the following leader-to-follower transition) that is at the origin of the detachment of rosette-shaped structures. This corresponds to the growth and location of the neuromasts along the two flanks of the embryo (see Figure 1 (a) below, from Lecaudey et al, 2008).

Our aim is to obtain a minimal mathematical model which is able to:

a) describe the collective cell migration, the formation and the detachment of the neuromasts, in the spatial and temporal scale of the experimental observations;
b) ensure the existence and stability of the rosette structures of the emerging neuromasts, as stationary solutions of the system.

Request a) will lead us to introduce in our model various effects, some of them experimentally evident (as chemotaxis, cell adhesion-repulsion, damping effects, chemical signals diffusion), others (as cell alignment, lateral inhibition mechanism, change of parameters in the mesenchymal-epithelial transition), biologically reasonable, introduced in order to reproduce observed results in literature. Request b), among other, allows us to obtain some important restrictions on the range of the values of some parameters of the model, which

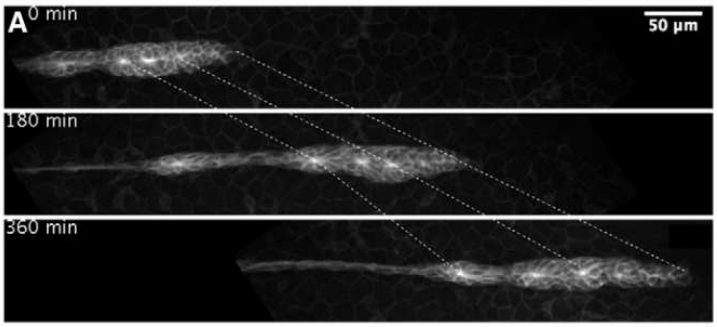

(a)

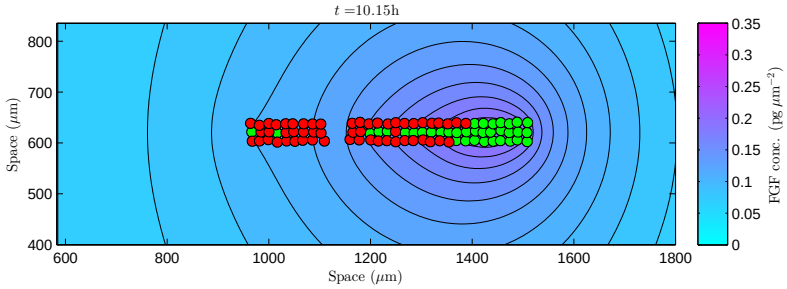

(b)

Fig. 1 (a) Image from a time-lapse movie about the migration in the zebrafish PLL primordium. Leading zone is on the right of the primordium, trailing zone is on the left. Cell migration is to the right while neuromasts deposition occurs in the trailing region (source from Lecaudey et al, 2008, reproduced with permission of Development). (b) An example of dynamical simulation of our mathematical model (see Section 5 for further details).

will be used in the numerical simulations of the dynamical case, other parameters being obtained from biological literature or by a numerical fitting. This aspect will be recovered in Section 6 and in Appendix A.

The model proposed here is a hybrid model: it describes cells as discrete entities and chemotactic molecules as continuous concentrations. This is a reasonable choice if we think that the total number of cells involved in the morphogenesis process is in the range 80–100 (Haas and Gilmour, 2006; Sarrazin et al, 2010). For analytical and computational simplicity in our analysis, here we consider only the 2D case, although we do not expect great changes passing to 3D, since experimental observations suggest that these phenomena involve only a thin cell layer. As we will see in more detail through numerical simulations given in Section 5, we can state that our mathematical model shows a substantial agreement with the biological observations and with the experimental data proposed in literature (Figure 1 (b), to be compared with (a)).

From a mathematical point of view, our model is based on a second order equation of the form

$$\ddot{\mathbf{X}}_i = \mathbf{F}(t, \mathbf{X}, \dot{\mathbf{X}}, u, \nabla u) - \mu \dot{\mathbf{X}}_i,$$

where $\mathbf{X}_i$, $i = 1, \ldots, N_{\text{tot}}$, is the position vector of the i-th cell, N_{tot} is the total number of cells, $\mathbf{X} := (\mathbf{X}_1, \ldots, \mathbf{X}_{N_{\text{tot}}})$, and $\dot{\mathbf{X}} := (\dot{\mathbf{X}}_1, \ldots, \dot{\mathbf{X}}_{N_{\text{tot}}})$. The function $\mathbf{F}$ includes several effects: from the detection of chemical signals u (chemotaxis, lateral inhibition) to mutual interactions between cells (alignment, adhesion, repulsion). All these effects take into account a non local sensing radius. In particular, we included an alignment term inspired by the Cucker-Smale mechanism (Cucker and Smale, 2007), though in our case it is coupled with other effects. A similar term has been applied in biological contexts by Szabò et al (2006), Arboleda-Estudillo et al (2010), and Sepúlveda et al (2013). The term $-\mu\dot{\mathbf{X}}_i$ represents damping due to cell adhesion to the substrate. Chemical signals are described using a reaction-diffusion equation

$$\partial_t u = D\Delta u + S(t, \mathbf{X}, u),$$

with a possible source or degradation term given in S. Finally the cell mesenchymal-epithelial differentiation in the primordium is performed by a switch variable, whose evolution in time is given by a suitable threshold function.

We will show that our model admits particular stationary solutions, biologically relevant and consistent with experimental observations. They correspond to the so called rosettes, that will form the future neuromasts. We investigate numerically their stability, finding in turn a nice agreement with biological evidences both in the stationary and in the dynamical setting.

A simplified attempt in the modelling of collective migration guided by chemical signals, tested on the lateral line formation in the zebrafish primordium, can be found in Streichan et al (2011). Although this model is proposed in full 2D framework, solutions are obtained only in 1D, and a limited number of effects is taken into account. In particular, only one type of cells is considered, i.e.: there is no differentiation in the cell state.

The paper is organized as follows: in Section 2 we recall some biological backgrounds and the phenomenology, based on the existing experimental observations. In Section 3 the mathematical model is introduced and its main features are discussed. In Section 4 we study the stationary configuration of the rosettes, and their stability. Section 5 deals with the dynamic model. We explain the methods used in the numerical simulations and some 2D numerical tests are presented, with the aim of illustrating the power and the limits of our approach. Section 6 is devoted to the conclusions. Finally, Appendix A contains the lists of main dimensional and nondimensional parameters used in the model.

2 Biological backgrounds

About zebrafish PLL, recent studies and experimental observations (Haas and Gilmour, 2006; Lecaudey et al, 2008; Nechiporuk and Raible, 2008) show an

initial elongated single group of cells in the otic vesicle, in which we can distinguish a *trailing region* near the head and a *leading region* oriented towards the future tail of the embryo. In the following few hours after the fertilization, a total cell migration begins posteriorly, from head to tail. Then the cells in the trailing region assemble into rosette structures (proto-neuromast), that are progressively deposited during the migration to form *neuromasts* (Nechiporuk and Raible, 2008) (see again Figure 1 (a)).

In general we can state two primary mechanisms that concur to this morphogenesis process: a collective migration, and a neuromasts assembly. About cell migration a very important role is played by chemokines as the *stromal cell-derived factor-1a* (*SDF-1a*) and its *CXCR4b* receptor (Ghysen and Chaudière, 2004; Haas and Gilmour, 2006). The former is expressed by the horizontal myoseptum, that separates the dorsal and ventral axial muscles, and acts as a haptotactic stripe for the migrating cells; the latter is expressed by the primordium itself (Li et al, 2004). Chemokine signaling is necessary to drive migration. In fact, it has been proved that, in absence of CXCR4b, cell movements are strongly uncoordinated, with a "zig zag" pattern, as can be seen performing kymograph analysis (see Haas and Gilmour, 2006). Moreover, next to the chemoattractant chemokine, migration within the primordium is guaranteed by a *cell-cell interaction*, exerted by an adhesion force via filopodia. This is confirmed by two observations in Haas and Gilmour (2006): firstly, cells lacking CXCR4b receptor, transplanted into wild-type primordium, preserve their migration through the contact with neighboring cells; secondly, even a small number of wild-type cells, transplanted in a mutant primordium (lacking the SDF-1a receptor), after moving themselves toward the leading edge can restore the collective migration. In this context other studies (Liu et al, 2003; Kerstetter et al, 2004; Papusheva and Heisenberg, 2010; Liu et al, 2011; Mertz et al, 2013) have shown that intercellular adhesion, typically through molecules as the cadherins, and *cell-substratum adhesion*, through integrins, have a crucial role in the spatial organization of tissues and in embryonic development. Integrin- and cadherin-mediated adhesion allows cells and tissues to respond to mechanical stimuli from their environment and to change shape without loosing integrity (Papusheva and Heisenberg, 2010, and references therein).

To understand the mechanism which drives the rosettes organization and neuromast deposition (a mechanism however not yet completely described, see Lecaudey et al, 2008), we have to make some considerations. Neuromast formation is strongly influenced by the concentration of *fibroblast growth factors* (*FGFs*) and their receptors *FGFRs* (Nechiporuk and Raible, 2008; Lecaudey et al, 2008). In zebrafishes, FGF signaling drives cells to assemble rosettes and gives rise to the subdivision of the lateral line. Among the 22 members of the FGF family, only FGF3 and FGF10 are expressed by the primordium (Böttcher and Niehrs, 2005), and they are substantially equivalent. In fact, inactivation of FGF3 or FGF10 alone does not alter significantly the development of the primordium, demonstrating a robustness of the system (Lecaudey et al, 2008). On the other hand, using a FGFR inhibitor SU5402, strongly affects the primordium: cells became disorganized and neuromast de-

position stops. In this case also the collective migration is compromised, probably due to an alteration also in CXCR4b receptors (Nechiporuk and Raible, 2008). Therefore, the rosette formation depends mainly on the total level of FGF and, as we will see below, on its location. We observe also that FGF and FGFR expressions are mutually exclusive, as confirmed by the location of their molecules: the former, broadly expressed in the leading region, and focused in one or two cells at the centre of the rosettes in the trailing region; the latter, at the same time, expressed in the trailing region except the FGF foci (Nechiporuk and Raible, 2008; Lecaudey et al, 2008). In the aim of designing a mathematical model, this suggests to divide the cell population into two groups: the *leader* mesenchymal cells (expressing FGF), and the *follower* epithelial cells (expressing FGFR). At the beginning, all the cells belong to the leading group. Afterwards some leaders in the trailing zone start to become followers, except one or two leader cells located in the centre, that maintain their mesenchymal state. Loss of FGF activity, on the contrary, implies that no transition can occurs (Lecaudey et al, 2008). Then, the follower cells are driven towards the FGF source to form a rosette. As a proto-neuromast becomes fully mature, it is deposited from the trailing edge, and a new rosette is formed again in a cyclic mechanism.

Let us now propose some rules that model the transition from a leader cell into a follower, corresponding to the activation of the FGFR receptor. We assume in the following that the transition occurs under three concomitant conditions:

1) a low level of SDF-1a (Ghysen and Chaudière, 2004);
2) a high level of FGF (Lecaudey et al, 2008);
3) influence of *lateral inhibition* (Haddon et al, 1998; Itoh and Chitnis, 2001; Hart et al, 2003; Matsuda and Chitnis, 2010; Mizoguchi et al, 2011; Sweet et al, 2011).

The first condition implies that rosette formation begins in the trailing region, where SDF-1a signal is already degraded by cells in the leading edge. The lateral inhibition in the third condition is a common phenomenon in embryology: a cell that adopts a particular feature (in this case the activation of FGFR receptor) inhibits its immediate neighbours from doing likewise. We propose to translate this condition considering leader-to-follower transition favored by a low number of cells in the neighbourhood. Condition 3), together with 2), implies that followers, activating FGFR receptor, inhibit the same activation in a central leader, so that it will express a significantly higher level of FGF signal (Lecaudey et al, 2008). Although other models can be imagined in relation with the lateral inhibition mechanism, this seems to be the most appropriate, and probably the simplest one, in order to obtain the observed structure of neuromasts. Finally, we remark that the leader-follower transition can be reversible, possibly with a time delay. In fact, blocking FGF activity makes all cells equally leader and causes the consequent melting of formed rosettes (Lecaudey et al, 2008).

In the following we will see that our mathematical model will be consistent with the biological observations if we consider chemical effects concomitant with other cell mechanisms, as lateral inhibition, alignment, damping and adhesion-repulsion effects.

3 The mathematical model

According to the above observations we propose a hybrid model which takes into account the difference between the cellular and the chemical scale. At the cellular level the model is discrete and includes the equation of motion and the equation of state leader-follower for each single cell, while at the molecular level the model is continuous and is based on the equations for the various chemical signals involved. Let us summarize the main ingredients which compose our model.

For cell motion we use a second order dynamic equation, which takes into account the forces acting on the cells. These forces are given by chemical signals and mechanical interaction between cells. Because of the equivalence between FGF3 and FGF10, we consider a single concentration and a single receptor, that we will denote respectively as FGF and FGFR. The SDF-1a effect is described by a haptotactic term produced by the gradient of the concentration of this chemokine, see Eisenbach and Lengeler (2004) for some biological backgrounds, while mathematical references can be found in Murray (2003) and Perthame (2007). In the same way, the action of FGFR on a follower cell is described by a chemotactic effect due to the gradient of the FGF produced by a leader cell.

Next we describe the cell-cell mechanical interactions due to filopodia, which consist in an alignment effect and both a radial attraction and repulsion depending on the relative position of the cells, see Mertz et al (2013) for experimental results in this direction. About alignment effects, we base our description on the seminal paper by Cucker and Smale (2007), while for the attraction-repulsion effects we refer to the mechanism introduced by D'Orsogna et al (2006); both effects are considered by Albi and Pareschi (2013). Finally, we introduce a damping term, proportional to the velocities, which models cell adhesion to the substrate (Rubinstein et al, 2009; Fournier et al, 2010; Bayly et al, 2012).

The follower-leader differentiation is represented mathematically by a switch state variable, which change its value according to the level of some related functions, which take into account the concentration of SDF-1a and of FGF and also the number of cells in a given neighbourhood of the given cell, as described in Section 2.

About the concentration of the FGF signal we associate a diffusion equation including a source term, given by the FGF production by the leader cells, and a natural molecular degradation term. The concentration of SDF-1a is described by an equation involving its degradation during the haptotactic process.

3.1 The basic mathematical model

Starting from the above considerations, we work in the following framework:

$$
\begin{aligned}
&\text{acceleration of } i\text{-th cell} = \text{haptotactic effect of SDF-1a}\\
&\qquad + \text{chemotactic effect of FGF source on the followers}\\
&\qquad + \text{cells alignment} + \text{cell adhesion and repulsion}\\
&\qquad + \text{damping effect}\\
&i\text{-th cell kind} = \begin{cases} \text{follower, if low level of SDF-1a} + \text{high level of FGF} \\ \qquad\qquad + \text{absence of lateral inhibition} \\ \text{leader,} \quad \text{otherwise} \end{cases}\\
&\text{rate of change of FGF signal} = \text{diffusion} + \text{production} + \text{molecular degradation}\\
&\text{rate of change of SDF-1a signal} = \text{degradation}
\end{aligned}
$$

Let $\mathbf{X}_i(t)$ be the position of a single i-th cell, $s(\mathbf{x},t)$ the SDF-1a concentration, $f(\mathbf{x},t)$ the total FGF concentration (including both FGF3 and FGF10), $\varphi_i(t)$ a variable that distinguishes a i-th cell to be, at time t, a leader ($\varphi_i(t)=1$) or a follower ($\varphi_i(t)=0$). We introduce the following equations:

$$
\begin{cases}
\ddot{\mathbf{X}}_i = \alpha \mathbf{F}_1\left(\nabla s\right) + \gamma(1-\varphi_i)\mathbf{F}_1\left(\nabla f\right) + \mathbf{F}_2(\dot{\mathbf{X}}) + \mathbf{F}_3(\mathbf{X}) \\
\qquad - \left[\mu_{\mathrm{F}} + (\mu_{\mathrm{L}} - \mu_{\mathrm{F}})\varphi_i\right]\dot{\mathbf{X}}_i, \\
\varphi_i = \begin{cases} 0, \text{ if } \delta F_1(s) - \left[k_{\mathrm{F}} + (k_{\mathrm{L}} - k_{\mathrm{F}})\varphi_i\right] F_1(h(f)) + \lambda \Gamma(n_i) \le 0, \\ 1, \quad \text{otherwise,} \end{cases} \\
\partial_t f = D\Delta f + \xi F_4(\mathbf{X}) - \eta f, \\
\partial_t s = -\sigma s F_5(\mathbf{X}),
\end{cases}
\tag{1}
$$

where α, γ, μ_{L}, μ_{F}, δ, k_{L}, k_{F}, λ, D, ξ, η, σ are given positive constants, and $F_n(\cdot)$, $n=1,\dots,5$, are suitable functions.

The term F_1, which is related to the detection of a chemical signal by i-th cell in its neighbourhood, is taken to be a weighted average over a ball of radius $\bar{R}$ and centred in $\mathbf{X}_i$:

$$
F_1(g(\mathbf{x},t)) := \frac{1}{W}\int_{\mathbf{B}(\mathbf{X}_i,\bar{R})} g(\mathbf{x},t) w_i(\mathbf{x})\, d\mathbf{x}, \tag{2}
$$

where

$$
\mathbf{B}(\mathbf{X}_i,\bar{R}) := \left\{\mathbf{x} : ||\mathbf{x}-\mathbf{X}_i|| \le \bar{R}\right\}, \tag{3}
$$

$||\cdot||$ being the Euclidean norm,

$$w_i(\mathbf{x}) := \begin{cases} 2\exp\left(-||\mathbf{x}-\mathbf{X}_i||^2 \dfrac{\log 2}{\bar{R}^2}\right) - 1, \text{ if } ||\mathbf{x}-\mathbf{X}_i|| \le \bar{R}; \\ 0, \qquad\qquad\qquad\qquad\qquad \text{otherwise;} \end{cases} \tag{4}$$

is a truncated Gaussian weight function, and

$$W := \int_{\mathbf{B}(\mathbf{X}_i,\bar{R})} w_i(\mathbf{x})\, d\mathbf{x}, \tag{5}$$

independently of i. A similar definition holds for the vector quantity $\mathbf{F}_1$. Reasonably we will choose $\bar{R}$ larger than the cell radius R (see Appendix A), so (2) describes a chemical signal that is sensed more in the centre of the cell and less at the edge of the cell extensions. The second term in $(1)_1$ refers to the attraction of a follower cell toward a source of FGF ligand. The switch variable φ_i makes this term zero for a leader cell that, expressing FGF, does not activate FGFR receptors (see Section 2).

The effect included in the third term of $(1)_1$ represents a possible cell alignment. For it we assume a Cucker-Smale-like *flocking term*:

$$\mathbf{F}_2(\dot{\mathbf{X}}) := \frac{1}{\bar{N}_i} \sum_{j:\mathbf{X}_j \in \mathbf{B}(\mathbf{X}_i,R_1)\setminus\{\mathbf{X}_i\}} \mathbf{H}(\dot{\mathbf{X}}_j - \dot{\mathbf{X}}_i). \tag{6}$$

Here R_1 is a suitable radius of influence,

$$\bar{N}_i := \operatorname{card}\{j : \mathbf{X}_j \in \mathbf{B}(\mathbf{X}_i, R_1)\}, \tag{7}$$

and the function $\mathbf{H}$ depends on the relative velocities $\dot{\mathbf{X}}_j - \dot{\mathbf{X}}_i$, i.e.:

$$\mathbf{H}(\dot{\mathbf{X}}_j - \dot{\mathbf{X}}_i) := [\beta_{\mathrm{F}} + (\beta_{\mathrm{L}} - \beta_{\mathrm{F}})\varphi_i\varphi_j] \frac{R_1^2}{R_1^2 + ||\mathbf{X}_j - \mathbf{X}_i||^2}(\dot{\mathbf{X}}_j - \dot{\mathbf{X}}_i), \tag{8}$$

β_{F}, β_{L} being constants. In particular we can have different coefficients of alignment for a leader or follower cell: the product $\varphi_i\varphi_j$ makes the coefficient equal to β_{F} if at least one of the two cell is follower ($\varphi_i\varphi_j = 0$) and equal to β_{L} in the case of two leaders ($\varphi_i\varphi_j = 1$). We remark that the flocking term given by (8), which is studied in Cucker and Smale (2007) and Ha and Liu (2009), in our model is coupled with other effects, as chemotaxis and attraction-repulsion effects (see below), and it is also computed on a truncated domain. Similar mechanisms, as given in (8), have been applied in biological contexts by Szabò et al (2006), Arboleda-Estudillo et al (2010), and Sepúlveda et al (2013), since the seminal paper of Vicsek et al (1995). In the following we will assume $R_1 = \bar{R}$ (see Appendix A), but in principle they can be different. In Appendix A we will give a justification for the introduction of an alignment term.

The function $\mathbf{F}_3$ includes adhesion-repulsion effects. In particular repulsion occurs at a distance between the centres of two cells less than R_4 and

takes into account the effects of a possible cell deformation. Conversely, adhesion occurs at a distance greater than R_4 and less than $R_5 > R_4$, and it is due to a mechanical interaction between cells via filopodia. We assume

$$\mathbf{F}_3(\mathbf{X}) := \sum_{j:\mathbf{X}_j \in \mathbf{B}(\mathbf{X}_i, R_5)\setminus\{\mathbf{X}_i\}} \mathbf{K}(\mathbf{X}_j - \mathbf{X}_i), \tag{9}$$

where the function $\mathbf{K}$ depends on the relative positions $\mathbf{X}_j - \mathbf{X}_i$, i.e.:

$$\mathbf{K}(\mathbf{X}_j - \mathbf{X}_i) := \begin{cases} -\omega_{\text{rep}} \left(\dfrac{1}{||\mathbf{X}_j - \mathbf{X}_i||} - \dfrac{1}{R_4} \right) \dfrac{\mathbf{X}_j - \mathbf{X}_i}{||\mathbf{X}_j - \mathbf{X}_i||}, \text{ if } ||\mathbf{X}_j - \mathbf{X}_i|| \le R_4; \\ \bar{\omega}_{\text{adh}} \left(||\mathbf{X}_j - \mathbf{X}_i|| - R_4 \right) \dfrac{\mathbf{X}_j - \mathbf{X}_i}{||\mathbf{X}_j - \mathbf{X}_i||}, \qquad \text{if } R_4 < ||\mathbf{X}_j - \mathbf{X}_i|| \le R_5; \end{cases} \tag{10}$$

with

$$\bar{\omega}_{\text{adh}} := \omega_{\text{adh,F}} + (\omega_{\text{adh,L}} - \omega_{\text{adh,F}})\varphi_i\varphi_j,$$

ω_{rep}, $\omega_{\text{adh,L}}$, $\omega_{\text{adh,F}}$ being constants. In practice we will choose $R_4 = 2R$ (see Appendix A), so that repulsion occurs when two cells start to be effectively overlapped. We note that function $(10)_1$ gives a repulsion which goes as $1/r$, r being the distance between the centres of two cells, as we can find in Cristiani et al (2011) and Colombi et al (2011). The function $(10)_2$ represents Hooke's law of elasticity, with different elastic coefficients for a leader cell and for a follower. In particular we have $\omega_{\text{adh,F}}$ if at least one of the two cells is a follower ($\varphi_i\varphi_j = 0$) and $\omega_{\text{adh,L}} > \omega_{\text{adh,F}}$ if two cells are both leaders ($\varphi_i\varphi_j = 1$). Similar terms can be found in Albi and Pareschi (2013), Joie et al (2013) and references therein. We remark that adhesion $(10)_2$ and alignment (8) produce different effects, though they both refer to a cell-cell interaction: the former a radial effect, the latter a tangential effect.

The last term in the first equation is due to the cell adhesion to the substrate (see for example Rubinstein et al, 2009; Fournier et al, 2010; Bayly et al, 2012), possibly with a different damping coefficient for a leader (μ_{L}, given by $\varphi_i = 1$) or a follower cell (μ_{F}, given by $\varphi_i = 0$).

The second equation in (1) defines the switch variable φ_i for the i-th cell. The leader-to-follower transition is performed requiring that the threshold function at the right hand side of $(1)_2$ is less than zero, according to the three conditions described in Section 2. For the FGF detection in $F_1(h(f))$ we choose the following form for the function $h(f)$:

$$h(f) := \frac{f}{f_{\max} + f}, \tag{11}$$

where $f_{\max}$ is constant. The function (11) includes a possible saturation effect when FGF molecules tend to occupy all receptors of a cell. The coefficients k_{L} and k_{F}, related respectively to a leader and a follower cell, provides a delay in the inverse follower-to-leader transition setting suitably $k_{\text{L}} < k_{\text{F}}$, this in accordance to observations in Section 2. About the lateral inhibition

mechanism, as proposed in Section 2, we introduce a function $\Gamma(n_i)$ that counts the number n_i of cells in a suitable neighbourhood of the i-th cell, with radius of influence R_2, namely

$$\Gamma(n_i) := \frac{e^{n_i}}{e^{n_i} + \Gamma_0} - \frac{1}{1 + \Gamma_0}, \tag{12}$$

where

$$n_i := \text{card}\left\{ j : \mathbf{X}_j \in \mathring{\mathbf{B}}(\mathbf{X}_i, R_2) \setminus \{\mathbf{X}_i\} \right\}, \tag{13}$$

Γ_0 is a constant, and $\mathring{\mathbf{B}}(\mathbf{X}_i, R_2)$ is the interior of $\mathbf{B}(\mathbf{X}_i, R_2)$. The function (12) is justified if we think of a neuromast as made by a single central leader and some followers around. In this context (12) takes very different values when it is evaluated on a central cell or on a cell on the boundary of the primordium. Moreover, it provides a fast saturation effect when n increases, so that a central leader perceives about the same inhibition effect from a certain value of n. This is useful to describe the possibility to obtain neuromasts with a variable number of cells, according to experimental observations (generally 8-12 cells) (Lecaudey et al, 2008). A suitable value for the constant Γ_0 is given in Appendix A, then we will choose the radius $R_2 = 2R$ in order to consider lateral inhibition as a pressure effect that occurs when two cells start to be overlapped.

In the diffusion equation $(1)_3$, only leader cells are responsible of the production of FGF, so that

$$F_4(\mathbf{X}) := \sum_{j=1}^{N_{\text{tot}}} \varphi_j \chi_{\mathbf{B}(\mathbf{X}_j, R_3)}, \tag{14}$$

where N_{tot} is the total number of cells, and

$$\chi_{\mathbf{B}(\mathbf{X}_j, R_3)} := \begin{cases} 1, \text{ if } \mathbf{x} \in \mathbf{B}(\mathbf{X}_j, R_3); \\ 0, \quad \text{otherwise.} \end{cases} \tag{15}$$

Similarly, in equation $(1)_4$ we take

$$F_5(\mathbf{X}) := \sum_{j=1}^{N_{\text{tot}}} \chi_{\mathbf{B}(\mathbf{X}_j, R_3)},$$

in which the variable φ_i does not appear now, because both leaders and followers are involved in the haptotactic process. Typically, we will choose $R_3 = R$ considering that the source of FGF and the degradation of SDF-1a signal is substantially defined by the dimension of a single cell (see Appendix A).

The above observations let us to summarize the following model:

$$
\begin{cases}
\ddot{\mathbf{X}}_i &= \dfrac{\alpha}{W}\displaystyle\int_{\mathbf{B}(\mathbf{X}_i,\bar{R})} \nabla s(\mathbf{x},t) w_i(\mathbf{x})\,d\mathbf{x} + \dfrac{\gamma(1-\varphi_i)}{W}\int_{\mathbf{B}(\mathbf{X}_i,\bar{R})} \nabla f(\mathbf{x},t) w_i(\mathbf{x})\,d\mathbf{x} \\
&\quad + \dfrac{1}{\bar{N}_i}\displaystyle\sum_{j:\mathbf{X}_j\in\mathbf{B}(\mathbf{X}_i,R_1)\setminus\{\mathbf{X}_i\}} \mathbf{H}(\dot{\mathbf{X}}_j-\dot{\mathbf{X}}_i) + \sum_{j:\mathbf{X}_j\in\mathbf{B}(\mathbf{X}_i,R_5)\setminus\{\mathbf{X}_i\}} \mathbf{K}(\mathbf{X}_j-\mathbf{X}_i) \\
&\quad - [\mu_{\mathrm{F}} + (\mu_{\mathrm{L}}-\mu_{\mathrm{F}})\varphi_i]\,\dot{\mathbf{X}}_i, \\
\varphi_i &= \begin{cases} 0, \text{ if } \dfrac{\delta}{W}\displaystyle\int_{\mathbf{B}(\mathbf{X}_i,\bar{R})} s(\mathbf{x},t) w_i(\mathbf{x})\,d\mathbf{x} \\ \qquad - \dfrac{k_{\mathrm{F}}+(k_{\mathrm{L}}-k_{\mathrm{F}})\varphi_i}{W}\displaystyle\int_{\mathbf{B}(\mathbf{X}_i,\bar{R})} \dfrac{f(\mathbf{x},t)}{f_{\max}+f(\mathbf{x},t)} w_i(\mathbf{x})\,d\mathbf{x} + \lambda\Gamma(n_i) \le 0, \\ 1, \quad \text{otherwise,} \end{cases} \\
\partial_t f &= D\Delta f + \xi\displaystyle\sum_{j=1}^{N_{\mathrm{tot}}} \varphi_j \chi_{\mathbf{B}(\mathbf{X}_j,R_3)} - \eta f, \\
\partial_t s &= -\sigma s \displaystyle\sum_{j=1}^{N_{\mathrm{tot}}} \chi_{\mathbf{B}(\mathbf{X}_j,R_3)},
\end{cases}
\tag{16}
$$

where the functions $\mathbf{H}(\dot{\mathbf{X}}_j-\dot{\mathbf{X}}_i)$ and $\mathbf{K}(\mathbf{X}_j-\mathbf{X}_i)$ are given by (8) and (10). Initial and boundary conditions have to be specified. For the i-th cell we set

$$
\mathbf{X}_i(0) = \mathbf{X}_{i0}; \quad \text{and} \quad \dot{\mathbf{X}}_i(0) = \mathbf{0}, \quad i = 1,\dots,N_{\mathrm{tot}}, \tag{17}
$$

together with the equally initial cell state of leader:

$$
\varphi_i(0) = 1, \quad i = 1,\dots,N_{\mathrm{tot}}. \tag{18}
$$

Now, let $\Omega = [a,b]\times[c,d]$ our domain, for FGF signal we require zero initial concentration and homogeneous Neumann boundary condition:

$$
f(\mathbf{x},0) = 0; \quad \frac{\partial f}{\partial \mathbf{n}} = 0, \quad \text{on } \partial\Omega. \tag{19}
$$

No-flow boundary condition $(19)_2$ is justified if we think of an experiment in which our domain is isolated from the surrounding environment. Then, since initially SDF-1a is only located in a given region

$$
s(\mathbf{x},0) = s_0(\mathbf{x}), \tag{20}
$$

where $s_0(\mathbf{x})$ has compact support in Ω. In particular we consider a rectangular stripe of width $2l$, $[\bar{a},\bar{b}]\times[m-l,m+l]$, with $[\bar{a},\bar{b}]\subset[a,b]$, $m=(c+d)/2$, and

$$
s_0(x,y) := \Phi(x)\Psi(y), \tag{21}
$$

where, for instance, we choose

$$\Phi(x) := \frac{s_{\max}}{2}\left[\tanh\left(\frac{x-c_1}{c_2}\right)+1\right]\chi_{[\bar{a},\bar{b}]}, \tag{22}$$

$s_{\max}$ is the initial maximum SDF-1a concentration, c_1, c_2 are constants. The function (22) yields a non uniform haptotactic gradient, that is stronger at the beginning and then tends to saturate when cells acquire enough velocity. Values for c_1, c_2 will be given in Section 5. Then we set

$$\Psi(y) := u_\varepsilon(y) * \chi_{[m-l,m+l]}(y) = \int_c^d u_\varepsilon(y-\tau)\chi_{[m-l,m+l]}(y)\,d\tau, \tag{23}$$

the convolution of $\chi_{[m-l,m+l]}(y)$ with a positive and symmetric mollifier

$$u_\varepsilon(y) := \begin{cases} \dfrac{1}{J}\dfrac{1}{\varepsilon}\, e^{-\dfrac{1}{1-(y/\varepsilon)^2}}, \text{ if } -\varepsilon < y < \varepsilon; \\ 0, \qquad\qquad\qquad \text{otherwise;} \end{cases} \tag{24}$$

where

$$J := \int_{-\varepsilon}^{\varepsilon} \frac{1}{\varepsilon}\, e^{-\dfrac{1}{1-(y/\varepsilon)^2}}\, dy, \tag{25}$$

is the normalization factor. The mollifier (24) is introduced to have sufficient smoothness for $s_0(\mathbf{x})$. A suitable value for the positive constant ε will be given in Section 5.

Although we have introduced an initial gradient for SDF-1a, we have tested in our simulations that the cells of the primordium can self-generate their own gradient, so the collective migration can be ensured, with a reduced velocity, even fixing a constant initial data for the SDF1-1a signal. Biological studies in this regard have been performed recently by Donà et al (2013). Anyway we find that an initial gradient for the SDF-1a signal is necessary to reach a cell velocity consistent with the experimental data (see also Appendix A).

3.2 The nondimensional model

Though we tend to use dimensional times and distances in the plots for easier comparison with experiments, the qualitative behaviour of the model (16) is more clearly described using a nondimensional form based on the following

dimensionless quantities:

$$t^* := \frac{t}{T}, \quad \mathbf{x}^* := \frac{\mathbf{x}}{R}, \quad \mathbf{X}^* := \frac{\mathbf{X}}{R}, \quad f^* := \frac{f}{f_{\max}}, \quad s^* := \frac{s}{s_{\max}},$$
$$W^* := \frac{W}{R^2}, \quad R_i^* := \frac{R_i}{R} \quad i = 1, \dots, 5, \quad \bar{R}^* := \frac{\bar{R}}{R},$$
$$\alpha^* := \frac{\alpha s_{\max} T^2}{R^2}, \quad \beta_{\mathrm{L}}^* := \beta_{\mathrm{L}} T, \quad \beta_{\mathrm{F}}^* := \beta_{\mathrm{F}} T, \quad \gamma^* := \frac{\gamma f_{\max} T^2}{R^2}, \quad \omega_{\mathrm{rep}}^* := \frac{\omega_{\mathrm{rep}} T^2}{R^2},$$
$$\omega_{\mathrm{adh,L}}^* := \omega_{\mathrm{adh,L}} T^2, \quad \omega_{\mathrm{adh},F}^* := \omega_{\mathrm{adh,F}} T^2, \quad \mu_L^* := \mu_{\mathrm{L}} T, \quad \mu_{\mathrm{F}}^* := \mu_{\mathrm{F}} T, \quad \delta^* := \frac{\delta s_{\max}}{\lambda},$$
$$k_{\mathrm{L}}^* := \frac{k_{\mathrm{L}}}{\lambda}, \quad k_{\mathrm{F}}^* := \frac{k_{\mathrm{F}}}{\lambda}, \quad D^* := \frac{DT}{R^2}, \quad \xi^* := \frac{\xi T}{f_{\max}}, \quad \eta^* := \eta T,$$
$$\sigma^* := \sigma T, \quad c_1^* := \frac{c_1}{R}, \quad c_2^* := \frac{c_2}{R}, \quad \varepsilon^* := \frac{\varepsilon}{R},$$

where T a characteristic time (see Appendix A). With these definitions, and maintaining for simplicity the asterisks only for the nondimensional constants, we have

$$\begin{cases} \ddot{\mathbf{X}}_i = \dfrac{\alpha^*}{W} \displaystyle\int_{\mathbf{B}(\mathbf{X}_i, \bar{R}^*)} \nabla s(\mathbf{x}, t) w_i(\mathbf{x})\, d\mathbf{x} + \dfrac{\gamma^*(1-\varphi_i)}{W} \displaystyle\int_{\mathbf{B}(\mathbf{X}_i, \bar{R}^*)} \nabla f(\mathbf{x}, t) w_i(\mathbf{x})\, d\mathbf{x} \\ \qquad + \dfrac{1}{\bar{N}_i} \displaystyle\sum_{j:\mathbf{X}_j \in \mathbf{B}(\mathbf{X}_i, R_1^*) \setminus \{\mathbf{X}_i\}} \mathbf{H}(\dot{\mathbf{X}}_j - \dot{\mathbf{X}}_i) + \displaystyle\sum_{j:\mathbf{X}_j \in \mathbf{B}(\mathbf{X}_i, R_5^*) \setminus \{\mathbf{X}_i\}} \mathbf{K}(\mathbf{X}_j - \mathbf{X}_i) \\ \qquad - \left[\mu_{\mathrm{F}}^* + (\mu_{\mathrm{L}}^* - \mu_{\mathrm{F}}^*)\varphi_i\right] \dot{\mathbf{X}}_i, \\ \varphi_i = \begin{cases} 0, \text{ if } \dfrac{\delta^*}{W} \displaystyle\int_{\mathbf{B}(\mathbf{X}_i, \bar{R}^*)} s(\mathbf{x}, t) w_i(\mathbf{x})\, d\mathbf{x} \\ \qquad - \dfrac{k_{\mathrm{F}}^* + (k_{\mathrm{L}}^* - k_{\mathrm{F}}^*)\varphi_i}{W} \displaystyle\int_{\mathbf{B}(\mathbf{X}_i, \bar{R}^*)} \dfrac{f(\mathbf{x}, t)}{1 + f(\mathbf{x}, t)} w_i(\mathbf{x})\, d\mathbf{x} + \Gamma(n_i) \le 0, \\ 1, \quad \text{otherwise}, \end{cases} \\ \partial_t f = D^* \Delta f + \xi^* \displaystyle\sum_{j=1}^{N_{\mathrm{tot}}} \varphi_j \chi_{\mathbf{B}(\mathbf{X}_j, R_3^*)} - \eta^* f, \\ \partial_t s = -\sigma^* s \displaystyle\sum_{j=1}^{N_{\mathrm{tot}}} \chi_{\mathbf{B}(\mathbf{X}_j, R_3^*)}, \end{cases} \tag{26}$$

where $w_i(\mathbf{x})$ and W are given by (4)–(5) replacing $\bar{R}$ with $\bar{R}^*$, then

$$\Gamma(n_i) := \frac{e^{n_i}}{e^{n_i} + \Gamma_0} - \frac{1}{1 + \Gamma_0}, \tag{27}$$

$$n_i := \mathrm{card}\left\{ j : \mathbf{X}_j \in \mathring{\mathbf{B}}(\mathbf{X}_i, R_2^*) \setminus \{\mathbf{X}_i\} \right\}, \tag{28}$$

$$\mathbf{H}(\dot{\mathbf{X}}_j - \dot{\mathbf{X}}_i) := \left[\beta_{\mathrm{F}}^* + (\beta_{\mathrm{L}}^* - \beta_{\mathrm{F}}^*)\varphi_i \varphi_j\right] \frac{R_1^{*2}}{R_1^{*2} + ||\mathbf{X}_j - \mathbf{X}_i||^2} (\dot{\mathbf{X}}_j - \dot{\mathbf{X}}_i), \tag{29}$$

and

$$\mathbf{K}(\mathbf{X}_j - \mathbf{X}_i) := \begin{cases} -\omega^*_{\text{rep}} \left(\dfrac{1}{||\mathbf{X}_j - \mathbf{X}_i||} - \dfrac{1}{R^*_4} \right) \dfrac{\mathbf{X}_j - \mathbf{X}_i}{||\mathbf{X}_j - \mathbf{X}_i||}, \text{ if } ||\mathbf{X}_j - \mathbf{X}_i|| \leq R^*_4; \\ \\ \bar{\omega}^*_{\text{adh}} \left(||\mathbf{X}_j - \mathbf{X}_i|| - R^*_4 \right) \dfrac{\mathbf{X}_j - \mathbf{X}_i}{||\mathbf{X}_j - \mathbf{X}_i||}, \qquad \text{if } R^*_4 < ||\mathbf{X}_j - \mathbf{X}_i|| \leq R^*_5; \end{cases} \tag{30}$$

with

$$\bar{\omega}^*_{\text{adh}} := \omega^*_{\text{adh,F}} + (\omega^*_{\text{adh,L}} - \omega^*_{\text{adh,F}})\varphi_i\varphi_j.$$

Initial and boundary conditions are still given by (17)–(23). In particular in (22), (24), and (25) we have to replace $s_{\max}$, c_1, c_2 and ε, with $s^*_{\max} = 1$, c^*_1, c^*_2 and ε^*.

4 Steady states and stability

Now we will investigate particular steady states for our model. They are biologically relevant, because they correspond to the neuromasts basic structure (see Section 2). This will be useful also to provide us a range of variability for some parameters or to specify some of their ratios. First we consider the stationary form of system (26)

$$\begin{cases} \dfrac{\gamma^*(1-\varphi_i)}{W} \displaystyle\int_{\mathbf{B}(\mathbf{X}_i, \bar{R}^*)} \nabla f(\mathbf{x}) w_i(\mathbf{x})\, d\mathbf{x} + \sum_{j:\mathbf{X}_j \in \mathbf{B}(\mathbf{X}_i, R^*_5)\setminus\{\mathbf{X}_i\}} \mathbf{K}(\mathbf{X}_j - \mathbf{X}_i) = \mathbf{0}, \\ \\ \varphi_i = \begin{cases} 0, \text{ if } -\dfrac{k^*_{\text{F}} + (k^*_{\text{L}} - k^*_{\text{F}})\varphi_i}{W} \displaystyle\int_{\mathbf{B}(\mathbf{X}_i, \bar{R}^*)} \frac{f(\mathbf{x})}{1+f(\mathbf{x})} w_i(\mathbf{x})\, d\mathbf{x} + \Gamma(n_i) \leq 0, \\ \\ 1, \quad \text{otherwise}, \end{cases} \\ \\ D^* \Delta f = \eta^* f - \xi^* \displaystyle\sum_{j=1}^{N_{\text{tot}}} \varphi_j \chi_{\mathbf{B}(\mathbf{X}_j, R^*_3)}, \\ \\ s = 0, \end{cases} \tag{31}$$

with

$$\frac{\partial f}{\partial \mathbf{n}} = 0, \quad \text{on } \partial\Omega.$$

Then we give the following

Definition 1 *We will call* N-rosette *($N \geq 2$) a configuration formed by a leader cell surrounded by N follower cells with their centres located on the vertices of a regular polygon of N sides (or a segment if $N = 2$) centred in the leader cell (Figure 2 (a)).*

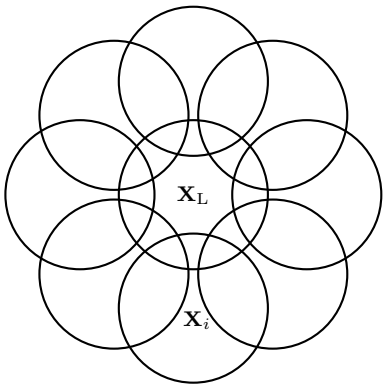

(a)

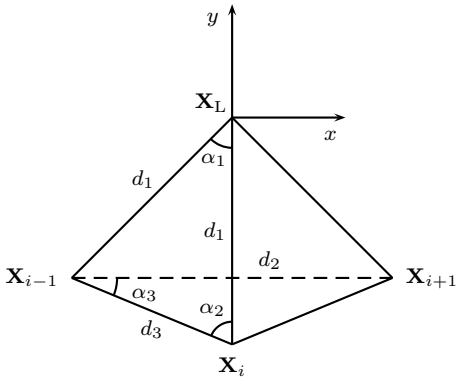

(b)

Fig. 2 (a) Example of 8-rosette with a leader centred in $\mathbf{X}_\mathrm{L}$ and 8 followers centred in $\mathbf{X}_i$, $i = 1, \ldots, 8$. (b) Geometrical configuration of a N-rosette with a leader cell centred in $\mathbf{X}_\mathrm{L}$ and some followers centred in $\mathbf{X}_{i-1}$, $\mathbf{X}_i$, $\mathbf{X}_{i+1}$.

With reference to Figure 2 (b), we call $\mathbf{X}_\mathrm{L}$ the centre of the leader cell, $\mathbf{X}_i$ the centre of a follower, d_1 the distance between the followers and the leader, d_2 the distance between two followers in alternating position (e.g. $\mathbf{X}_{i-1}$ and $\mathbf{X}_{i+1}$), d_3 the distance between two adjoining followers (e.g. $\mathbf{X}_i$ and $\mathbf{X}_{i+1}$), and α_1, α_2, α_3 the angles in the figure.

By symmetry considerations we set:

$$\alpha_1 = \frac{2\pi}{N}, \quad \alpha_2 = \frac{\pi - \alpha_1}{2}, \quad \alpha_3 = \frac{\pi}{2} - \alpha_2 = \frac{\pi}{N}, \tag{32}$$

$$d_2 = 2d_1 \sin\frac{2\pi}{N}, \tag{33}$$

$$d_3 = 2d_1 \sin\frac{\pi}{N}. \tag{34}$$

Now we assume the following physically reasonable hypotheses for a N-rosette:

1) the range of lateral inhibition is equal to the range of repulsion between cells:

$$R_2 = R_4; \tag{35}$$

2) the followers are located in the range of the lateral inhibition of the leader:

$$d_1 \leq R_2; \tag{36}$$

3) there is no repulsion between adjoining followers if $N = 2, 3$:

$$d_3 \geq R_4; \tag{37}$$

there is no repulsion between followers in alternating position if $N \geq 4$:

$$d_2 \geq R_4. \tag{38}$$

We point out that Hypothesis 1) is justified if we think of repulsion and lateral inhibition both due to the pressure between cell membranes. Hypothesis 2) is a direct consequence of the definition of a N-rosette. Finally, Hypothesis 3) ensures that repulsion, seen as a pressure effect, can be exerted only by adjacent cells, and not bypassing a single cell or considering cells completely overlapped. In particular in Hypothesis 3), for $N = 2, 3$, followers in alternating position coincide respectively with the same cell and with adjoining followers, this justifies (37).

Taking system (31) and Hypotheses (35)–(38) into account, we can state the following results.

Proposition 1 *There exist N-rosettes if and only if $N \leq 12$. Moreover the distance d_1, depending on N, can vary in the following ranges:*

$$\frac{1}{2\sin\frac{\pi}{N}} \leq \frac{d_1}{R_4} \leq 1, \quad \textit{if} \quad N = 2, 3, \tag{39}$$

$$\frac{1}{2\sin\frac{2\pi}{N}} \leq \frac{d_1}{R_4} \leq 1, \quad \textit{if} \quad 4 \leq N \leq 12. \tag{40}$$

Proof. Condition (39) is a consequence of (36), (35), (37), and (34). While (40) is a consequence of (36), (35), (38), and (33). In particular (40) is not empty if and only if $N \leq 12$.

The maximum number of cells, which is provided by the previous proposition, is consistent with the experimental observations as shown in Lecaudey et al (2008).

Proposition 2 *In a N-rosette there are repulsion and lateral inhibition effects between adjoining followers if and only if $N \geq 4$. In particular if $N \geq 6$ these effects do not depend on d_1, and if $N = 4, 5$ this holds if and only if*

$$\frac{1}{2\sin\frac{2\pi}{N}} \leq \frac{d_1}{R_4} < \frac{1}{2\sin\frac{\pi}{N}}, \quad N = 4, 5. \tag{41}$$

Proof. Hypothesis 1) ensures that this proof holds both for repulsion and lateral inhibition effects. If $N = 2, 3$ the statement is true thanks to Hypothesis 3). If $N \geq 6$ from (34), (35), and (36) we have

$$d_3 \leq d_1 \leq R_2 = R_4,$$

independently from d_1.
If $N = 4, 5$, using (34) we have repulsion if and only if

$$d_3 = 2d_1 \sin\frac{\pi}{N} < R_4. \tag{42}$$

From (42) and (40) equation (41) follows.

Now, in order to fix the range of variability for some parameters we solve the nondimensional system (31) for a N-rosette with a leader in $\mathbf{X}_\mathrm{L}$, setting a frame centred $\mathbf{X}_\mathrm{L}$ with axes passing through the centre of a follower (Figure 2 (b)). For simplicity we introduce the following symbols:

$$\overline{\nabla f(\mathbf{X}_i)} := \frac{1}{W}\int_{\mathbf{B}(\bar{R}^*,\mathbf{X}_i)} \nabla f(\mathbf{x}) w_i(\mathbf{x})\, d\mathbf{x},$$
$$\overline{\overline{f(\mathbf{X}_i)}} := \frac{1}{W}\int_{\mathbf{B}(\bar{R}^*,\mathbf{X}_i)} \frac{f(\mathbf{x})}{1+f(\mathbf{x})} w_i(\mathbf{x})\, d\mathbf{x},$$

to denote the weighted average of the functions ∇f and $\frac{f}{1+f}$.

Firstly, equation $(31)_2$ for each follower and for the leader becomes respectively:

$$\varphi_i = 0 \Leftrightarrow -k_\mathrm{F}^* \overline{\overline{f(\mathbf{X}_i)}} + \Gamma(n) \leq 0, \quad i = 1, \ldots, N, \tag{43}$$
$$\varphi_0 = 1 \Leftrightarrow -k_\mathrm{L}^* \overline{\overline{f(\mathbf{X}_\mathrm{L})}} + \Gamma(N) > 0, \tag{44}$$

where the function Γ is given by (27). Here the number n, which is related to the lateral inhibition, is given by (28) and, by symmetry considerations, it does not depend on i. Moreover, according to Hypothesis 2) and Proposition 2, it takes only the values 1 or 3: if $N \geq 6$, or $N = 4, 5$ and holds condition (41), we have to take $n = 3$, otherwise $n = 1$. The case $n = 3$ means that on the i-th cell we have the lateral inhibition of the leader cell and of the two adjoining followers, while in the case $n = 1$ we have only the lateral inhibition of the leader cell. The other cases for n are not possible due to conditions (35)–(38) assumed on the distances.

Now, the function $f(\mathbf{x})$, which is needed in (43) and (44), is the solution in the domain Ω of equation $(31)_3$, with Neumann boundary condition, that in this case takes the form

$$D^*\Delta f - \eta^* f = -\xi^* \chi_{\mathbf{B}(\mathbf{X}_\mathrm{L}, R_3^*)}, \tag{45}$$

$$\frac{\partial f}{\partial \mathbf{n}} = 0, \quad \text{on } \partial\Omega, \tag{46}$$

$\mathbf{X}_\mathrm{L}$ being the centre of the leader cell, the only one that produces FGF signal. If Ω is a circular domain centred in the leader cell, radial symmetry of the solution of (45) and (46) implies the quantities $\overline{\overline{f(\mathbf{X}_i)}}$ to be the same for all i, so that (43) and (44) become

$$k_\mathrm{F}^* \geq \bar{k}_\mathrm{F}^* := \Gamma(n)/\overline{\overline{f(\mathbf{X}_i)}}, \tag{47}$$

$$k_\mathrm{L}^* < \bar{k}_\mathrm{L}^* := \Gamma(N)/\overline{\overline{f(\mathbf{X}_\mathrm{L})}}. \tag{48}$$

Now we try to obtain a numerical estimate for the bound functions $\bar{k}_\mathrm{F}^*$ and $\bar{k}_\mathrm{L}^*$, as N changes. We set a domain $\Omega = [0, 200] \times [0, 200]$ (μm^2) with a single leader cell located in $\mathbf{X}_\mathrm{L} = (100, 100)$ (μm). We choose the square domain size sufficiently large, so that its influence on the solution can be neglected in the time period of interest. Then equations (45) and (46) are numerically solved in such a domain, as described in Section 5.1 and Appendix B to follow, using a spatial discretization corresponding to $\Delta x = \Delta y = 0.2$ μm. Parameters D^*, η^*, ξ^*, R_2^*, R_3^*, R_4^*, $\bar{R}^*$ used here are listed in Table 3, Appendix A.

Figure 3 shows a numerical estimate for the lower bound $\bar{k}_\mathrm{F}^*$ in (47). For each fixed value of N, $N = 2, \ldots, 12$, the curve indicates the value of $\bar{k}_\mathrm{F}^*$ as a functions of d_1, which is the distance between leader and follower. In practice, taking into account a N-rosette configuration as in Figure 2 (b), the numerical value of $f(\mathbf{x})$ is used to compute $\overline{\overline{f(\mathbf{X}_i)}}$ as the distance d_1 from $\mathbf{X}_i$ to $\mathbf{X}_\mathrm{L}$, suitably discretized, changes. Depending on the number of cells that make lateral inhibition on $\mathbf{X}_i$, also the numerator $\Gamma(n)$, can vary, for a fixed N, with respect to d_1 as established by Proposition 2. Since the scale of the curves is essentially different as N changes, we present our results in two different pictures in Figure 3. Notice that the range of the distance d_1 to be considered depends on N according to (39) and (40) in Proposition 1: the starting point on the curve is marked by a "•", while the ending point is represented by $d_1 = R_4$ for all N. We have already observed that $\Gamma(n)$ can only obtain the values $\Gamma(1)$ or $\Gamma(3)$ according to Proposition 2. So, clearly, the curves for $N = 2, 3$ are overlapped (Figure 3 (a)), the same for $N = 6, \ldots, 12$ (Figure 3 (b)). For $N = 4, 5$ the curves start in Figure 3 (b), when $\Gamma(n) = \Gamma(3)$, until $d_1 \approx 14$ μm for $N = 4$, and $d_1 \approx 17$ μm for $N = 5$ (markers "×"), then $\Gamma(n)$ becomes $\Gamma(1)$ and, for larger values of d_1, the curves continue in Figure 3 (a). For $N = 12$ the right hand side of (47) assumes a single value in $d_1 = R_4$ in Figure 3 (b).

On the other hand, using again the numerical solution of $f(\mathbf{x})$, the right hand side of (48) can be tabulated as N changes. Its values are given in Table 1.

Table 1 Numerical values of the upper bound $\bar{k}_{\mathrm{L}}^{*}$ in (48) for $N = 2, \ldots, 12$. In practice fixing N we have the upper bound of k_{L}^{*} for the existence of a steady N-rosette.

N	$\bar{k}_{\mathrm{L}}^{*}$ (nondim.)	N	$\bar{k}_{\mathrm{L}}^{*}$ (nondim.)
2	0.6707	8	1.8187
3	1.1580	9	1.8230
4	1.5146	10	1.8245
5	1.6987	11	1.8251
6	1.7769	12	1.8253
7	1.8073		

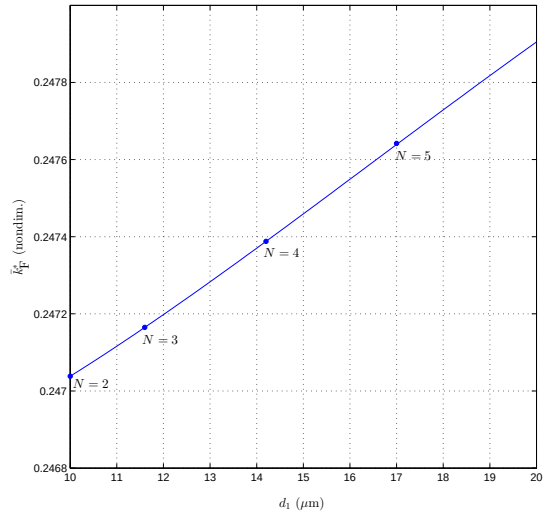

(a)

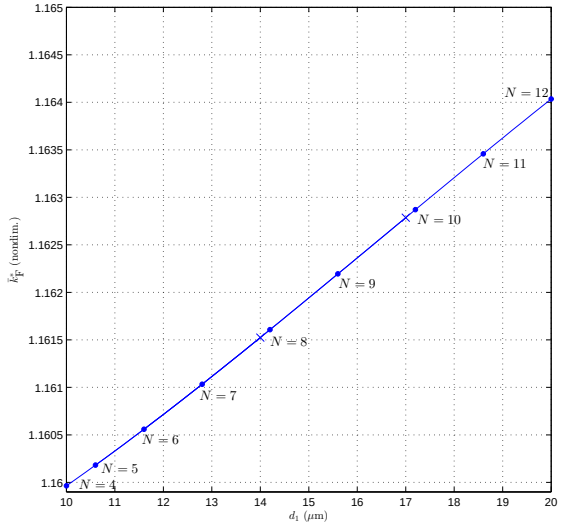

(b)

Fig. 3 Numerical plot of the lower bound $\bar{k}_F^*$ in (47) as a function of d_1. The curve gives the lower bound for k_F^* for a fixed N and d_1. Since the scale of the curves is essentially different, we present in (a) the case $N = 2, 3$, in which the curves are overlapped, and similarly in (b) the case $N = 6, \ldots, 12$. The starting point on the curves is marked by "•", while the ending point is represented by $d_1 = R_4$ for all N. For $N = 4, 5$ the curves start in (b) until $d_1 \approx 14$ μm and $d_1 \approx 17$ μm respectively (markers "×"), then for larger values of d_1 they continue in (a). For $N = 12$ the curve is reduced to a single value in $d_1 = R_4$ in (b).

Now, equation $(31)_1$ becomes

$$\sum_{j:\mathbf{X}_j\in\mathbf{B}(\mathbf{X}_\mathrm{L},R_5^*)\setminus\{\mathbf{X}_\mathrm{L}\}} \mathbf{K}(\mathbf{X}_j-\mathbf{X}_\mathrm{L})=\mathbf{0}, \tag{49}$$

$$\gamma^*\overline{\nabla f(\mathbf{X}_i)}+\sum_{j:\mathbf{X}_j\in\mathbf{B}(\mathbf{X}_i,R_4^*)\setminus\{\mathbf{X}_i\}} \mathbf{K}(\mathbf{X}_j-\mathbf{X}_i)=\mathbf{0},\quad i=1,\dots,N, \tag{50}$$

respectively for the leader and for each follower. Here $\mathbf{K}$ contains only repulsion term:

$$\mathbf{K}(\mathbf{X}_j-\mathbf{X}_i):=-\omega^*_{\mathrm{rep}}\left(\frac{1}{||\mathbf{X}_j-\mathbf{X}_i||}-\frac{1}{R_4^*}\right)\frac{\mathbf{X}_j-\mathbf{X}_i}{||\mathbf{X}_j-\mathbf{X}_i||}.$$

For symmetry (49) is identically satisfied. Then in (50) $f(\mathbf{x},t)$ is given by (45) and (46), so in a circular domain Ω we can write the same relation for all i. For example, in relation to Figure 2 (b), we have

$$\gamma^*\overline{\partial_y f(\mathbf{X}_i)}-\omega^*_{\mathrm{rep}}h_1(d_1^*)-\omega^*_{\mathrm{rep}}h_2(N,d_1^*)=0, \tag{51}$$

in which $\omega^*_{\mathrm{rep}}h_1(d_1^*)$ represents the repulsion of the leader:

$$h_1(d_1^*):=\frac{1}{d_1^*}-\frac{1}{R_4^*},$$

$d_1^*=d_1/R$ is the nondimensional value of d_1, and $\omega^*_{\mathrm{rep}}h_2(N,d_1^*)$ is the possible repulsion of two adjoining followers according to (34) and Propositions 1–2, namely:

$$h_2(N,d_1^*):=\begin{cases}0, & \text{if } N=2,3;\\ 2\left(\dfrac{1}{2d_1^*\sin\frac{\pi}{N}}-\dfrac{1}{R_4^*}\right)\sin\dfrac{\pi}{N}, & \text{if } N=4,5\wedge\frac{d_1^*}{R_4^*}<\frac{1}{2\sin\frac{\pi}{N}};\\ 0, & \text{if } N=4,5\wedge\frac{1}{2\sin\frac{\pi}{N}}\le\frac{d_1^*}{R_4^*}\le 1;\\ 2\left(\dfrac{1}{2d_1^*\sin\frac{\pi}{N}}-\dfrac{1}{R_4^*}\right)\sin\dfrac{\pi}{N}, & \text{if } 6\le N\le 12.\end{cases} \tag{52}$$

We remark that equation (51) is useful for two reasons. First, if we know an experimental value for the distance d_1^* we can obtain, fixing N, the ratio $\omega^*_{\mathrm{rep}}/\gamma^*$ as a function of d_1^*:

$$\frac{\omega^*_{\mathrm{rep}}}{\gamma^*}=\Theta_N(d_1^*):=\frac{\overline{\partial_y f(\mathbf{X}_i)}}{h_1(d_1^*)+h_2(N,d_1^*)}. \tag{53}$$

On the other hand, if Θ_N is invertible, we can express d_1^* as a function of ω^*_{rep} and γ^* that is the equilibrium distance for a N-rosette fixed the physical parameters.

Figure 4 represents a dimensional numerical plot of Θ_N for $N=2,\dots,12$. It shows that Θ_N is monotone with respect to d_1 for all N, so that relation

(53) is invertible. To obtain this plot the value of $f(\mathbf{x})$ has been obtained numerically from (45) and (46) as previously described, fixing the same domain and the same parameters. Then the right hand side of (53), for a fixed N, is computed on a discretized distance d_1^*, as done to obtain Figure 3. The domain of the curves, again as in Figure 3, is given by (39) and (40); now it represents the admissible distances d_1 for a N-rosette, as N changes. Symbol "•" marks the origin of the curves. For $N = 2, 3$ the curves are overlapped (first line in the top) because for them $h_2 = 0$ (see (53) and (52)). For $N = 4, 5$ the curves coincide with the curve $N = 2, 3$ when h_2 becomes zero. This happens about for $d_1 > 14$ μm for $N = 4$, and about for $d_1 > 17$ μm for $N = 5$, as we can see in $(52)_{2,3}$. The curves corresponding to $N = 2, \ldots, 6$ have a vertical asymptote in $d_1 = R_4$ where the functions h_1 and h_2 in (53) become zero. Conversely, for $N = 7, \ldots, 12$, Θ_N is defined in $d_1 = R_4$. In particular for $N = 12$, due to (40), the curve is reduced to a single value in $d_1 = R_4$ given by $\Theta_{12}(R_4)$ (marker "•" on the right).

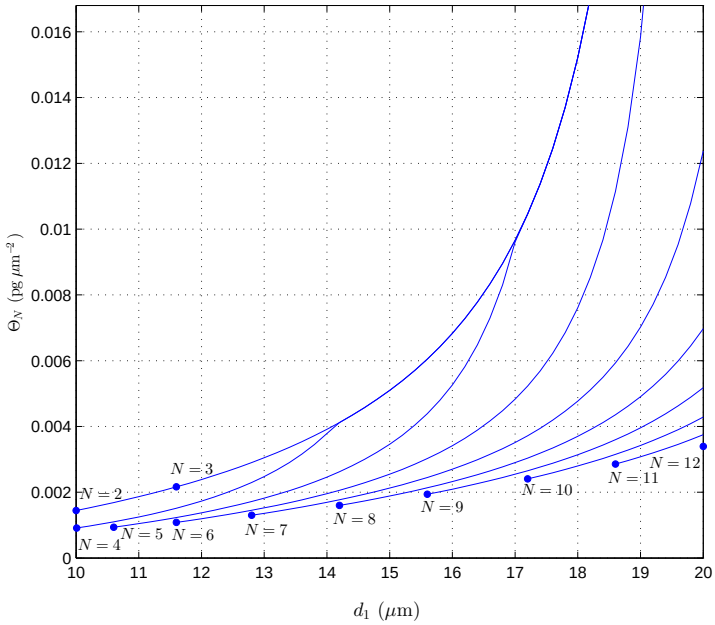

Fig. 4 Dimensional numerical plot of Θ_N for $N = 2, \ldots, 12$, that demonstrates that this function is monotone with respect to d_1 and then invertible. The first two curves, for $N = 2, 3$, coincide (first line in the top). Then, from the top to the bottom, we have the curves related to $N = 5, \ldots, 11$. For $N = 4, 5$ the curves go to coincide with the first curve on the top about from $d_1 > 14$ μm, and $d_1 > 17$ μm respectively. For $N = 12$ the curve is reduced to a single value in $d_1 = R_4$. In practice fixing N and d_1 we have the value of Θ_N that provides in (53) the ratio of the parameters ω^*_{rep} and γ^*.

Typical values for N and d_1 (or d_1^*) to be used in (47), (48), and (53) will be given in Appendix A.

Now, in order to test numerically a steady N-rosette, we perform a dynamic simulation of the model (26), as described in Section 5.1, with initial data given by a solution of the stationary system (31). With this type of simulations we verify that our numerical approximation scheme, discussed later in Appendix B, is adequate to keep the stationary solutions of our interest.

In particular, we consider the spatial domain $\Omega = [0, 200]\times[0, 200]$ (μm^2) and the time interval $[0, 50]$ (h), that is a typical time range used in the experimental observations (Nechiporuk and Raible, 2008). Spatial and temporal discretizations are respectively $\Delta x = \Delta y = 0.2\,\mu$m and $\Delta t = 0.01$ h. Initial data are set as follows:

$$\mathbf{X}_i(0) = \mathbf{X}_{i0}, \tag{54}$$

$\mathbf{X}_{i0}$ being a 8-rosette centred in $\mathbf{X}_{\mathrm{L}}(0) = (100, 100)$ (μm), with follower-leader distance fixed at $d_1 = \frac{3}{2}R$ (see Appendix A and Figure 5 (a)),

$$\dot{\mathbf{X}}_i(0) = \mathbf{0}, \tag{55}$$

$$f(\mathbf{x}, 0) = f_0(\mathbf{x}), \tag{56}$$

with $f_0(\mathbf{x})$ solution of equation $(31)_3$ with homogeneous Neumann boundary condition in the same domain,

$$s(\mathbf{x}, 0) = 0, \tag{57}$$

according to $(31)_4$. The parameters used here are listed in Appendix A (see Tables 2–3).

We see that our numerical results demonstrate that, with good approximation, the initial configuration stays constant in time. Figure 5 shows evolution in space of the dimensional solution at two different time steps: $t = 0$ h and $t = 50$ h. Green colour marks the leader cell ($\varphi_i = 1$), and red colour marks a follower cell ($\varphi_i = 0$). Contour plot in the background is related to the FGF signal concentration, while the variable $s(\mathbf{x}, t)$ is not shown. Figure 6 shows the evolution in time of the maximum relative error on the position,

$$E_{\mathrm{max,rel}}(t) := \frac{\max_{1\le i\le N_{\mathrm{tot}}} \|\mathbf{X}_i(t) - \mathbf{X}_{i0}\|}{R}, \tag{58}$$

and the maximum velocity

$$V_{\max}(t) := \max_{1\le i\le N_{\mathrm{tot}}} \left\|\dot{\mathbf{X}}_i(t)\right\|. \tag{59}$$

$E_{\mathrm{max,rel}}$ suggests a deviation from the initial position in the order of 10^{-3} times cell radius, while $V_{\max}$ is in the order of 10^{-4} μm h^{-1}, which is very small with respect to the cell velocity during migration that is around 69 μm/h (Lecaudey et al, 2008). Plots in Figure 5 are obtained computing, in our numerical simulation, quantities (58) and (59) at each time step.

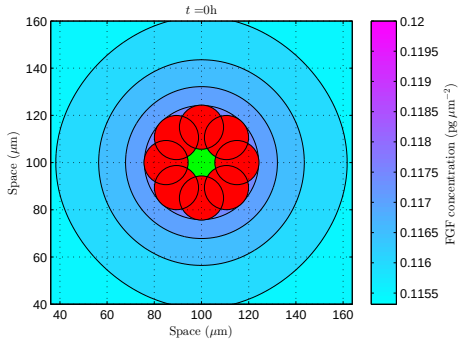

(a)

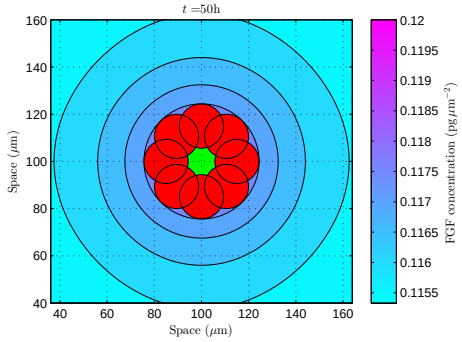

(b)

Fig. 5 Numerical simulation of a steady solution given by a 8-rosette. (a)-(b) are related respectively to the dimensional plot at two different time steps: $t = 0$ h and $t = 50$ h. System (26) is solved as described in Section 5.1 and Appendix B in $\Omega = [0, 200] \times [0, 200]$ (μm^2) (plot refers only to a part of the domain) and in $[0, 50]$ (h). Spatial and temporal discretization is set to $\Delta x = \Delta y = 0.2$ μm and $\Delta t = 0.01$ h. Initial data are given by (54)–(57). The parameters used here are listed in Appendix A. Green colour (●) marks the leader cell, red colour (●) a follower cell, contour plot in the background is the FGF signal concentration. Variable $s(\mathbf{x}, t)$ is not shown.

Now the stability of a N-rosette will be numerically investigated. Starting from the previous numerical test we perform a dynamic simulation perturbing the initial equilibrium configuration of the 8-rosette. Namely, each centre of a follower cell is translated of a ray vector whose magnitude and direction are random number in the interval $[0, 5]$ (μm) and $[0, 2\pi]$. Spatial domain and parameters are the same as in the previous simulation, while the time range is set to $[0, 60]$ (h).

Figure 7 shows the evolution in space of the dimensional solution at two time steps: $t = 0$ h and $t = 60$ h. Colour convention is the same as Figure 5. Figure 8 shows the evolution in time of the maximum relative error on the position $E_{\max,\mathrm{rel}}(t)$ and the maximum velocity $V_{\max}(t)$. $E_{\max,\mathrm{rel}}$ indicates a deviation from the initial position in the order of 10^{-1} times cell radius, and also

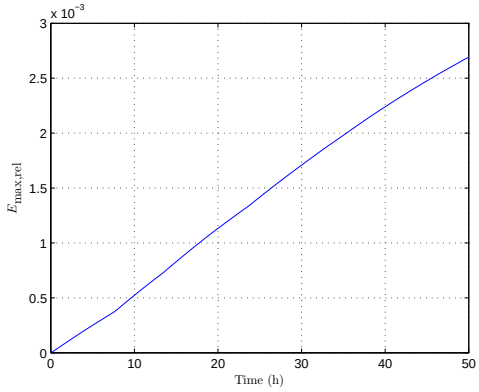

(a)

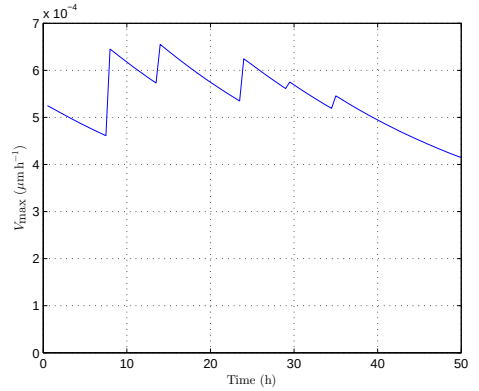

(b)

Fig. 6 Numerical assessment of a steady 8-rosette. (a) Plot in time of the maximum relative error $E_{\max,\mathrm{rel}}(t)$. (b) Plot of the maximum velocity $V_{\max}(t)$.

$V_{\max}$ is small, being in the order of 10^{-2} μm h^{-1}. Our data demonstrate that the equilibrium configuration of our 8-rosette is stable. Furthermore, numerical simulations show that similar results can hold also if $N \neq 8$, for instance for $N = 5$ or 10 (data not shown). We note that in a physically reasonable time range we do not observe the asymptotic stability of the rosette structures, which is actually not expected, but just the simple stability.

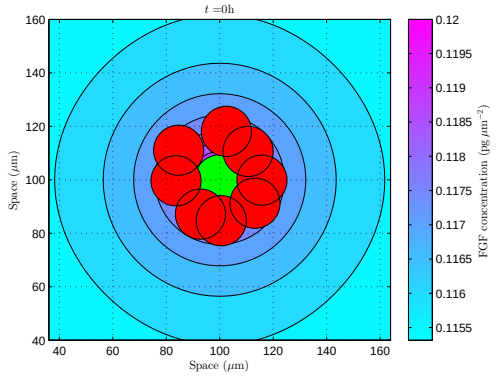

(a)

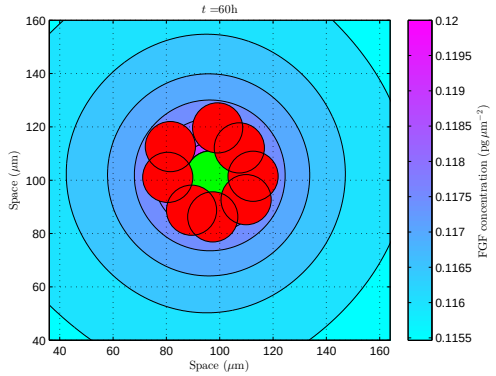

(b)

Fig. 7 Numerical assessment of stability of a 8-rosette. (a)-(b) are related respectively to the dimensional plot at $t = 0$ h and $t = 60$ h. System (26) is solved as described in Section 5.1 and Appendix B in $\Omega = [0, 200] \times [0, 200]$ (μm^2) (plot refers only to a part of the domain) and in $[0, 50]$ (h). Spatial and temporal discretization is the same as in Figure (5). Initial data are given by a perturbation of positions (54), and by (55)–(57). The parameters used here are listed in Appendix A. Green colour (●) marks the leader cell, red colour (●) a follower cell, contour plot in the background is the FGF signal concentration. Variable $s(\mathbf{x}, t)$ is not shown.

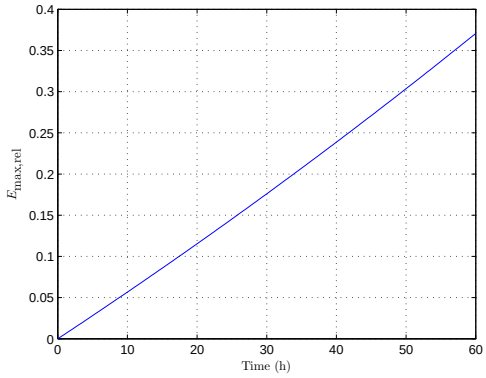

(a)

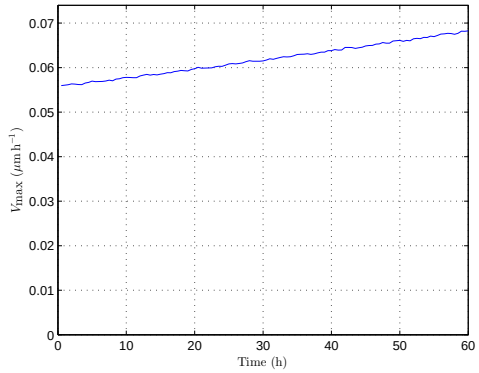

(b)

Fig. 8 Numerical assessment of stability of a 8-rosette. (a) Plot in time of the maximum relative error $E_{\max,\mathrm{rel}}(t)$. (b) Plot of the maximum velocity $V_{\max}(t)$.

5 Dynamic simulations

5.1 Numerical methods

All the numerical tests in the paper employ a 2D finite difference scheme with a uniform spatial and temporal grid.

About system (26), the equation for $\ddot{\mathbf{X}}$ is reduced to the first order system

$$\begin{cases} \dot{\mathbf{Y}}_i = \dfrac{\alpha^*}{W}\displaystyle\int_{\mathbf{B}(\mathbf{X}_i,\bar{R}^*)} \nabla s(\mathbf{x},t) w_i(\mathbf{x})\,d\mathbf{x} + \dfrac{\gamma^*(1-\varphi_i)}{W}\int_{\mathbf{B}(\mathbf{X}_i,\bar{R}^*)} \nabla f(\mathbf{x},t) w_i(\mathbf{x})\,d\mathbf{x} \\ \qquad + \dfrac{1}{\bar{N}_i}\displaystyle\sum_{j:\mathbf{X}_j\in\mathbf{B}(\mathbf{X}_i,R_1^*)\setminus\{\mathbf{X}_i\}} \mathbf{H}(\mathbf{Y}_j-\mathbf{Y}_i) + \sum_{j:\mathbf{X}_j\in\mathbf{B}(\mathbf{X}_i,R_5^*)\setminus\{\mathbf{X}_i\}} \mathbf{K}(\mathbf{X}_j-\mathbf{X}_i) \\ \qquad - \left[\mu_{\mathrm{F}}^* + (\mu_{\mathrm{L}}^*-\mu_{\mathrm{F}}^*)\varphi_i\right]\mathbf{Y}_i, \\ \dot{\mathbf{X}}_i = \mathbf{Y}_i. \end{cases} \tag{60}$$

Then equation $(60)_1$ is discretized with the one step IMEX method, putting totally implicit the terms in $\mathbf{Y}_i$ and $\mathbf{Y}_j$ at the right hand side, while totally explicit the other addends. Equation $(60)_2$ is solved with the forward Euler method.

About equation $(26)_3$ we use a classical exponential transformation in order to eliminate the stiff term $-\eta^* f$, and then we apply a central difference scheme in space and the parabolic Crank-Nicolson scheme in time, subject to zero flux boundary conditions. In practice, in the numerical simulations we choose the domain size sufficiently large that over the time period of interest have a negligible impact on the solution. Finally in equation $(26)_4$ the explicit Euler method is employed.

For further details about the numerical approximation scheme designed for system (26) we refer to Appendix B.

5.2 Numerical tests

Now we simulate the zebrafish lateral line growth in a two-dimensional space, during about 20 h. Using the numerical method proposed in Section 5.1 and Appendix B we solve system (26) in a domain $\Omega = [0, 5000] \times [0, 1240]$ (μm^2), with a spatial and temporal discretization given respectively by $\Delta x = \Delta y = 5\,\mu$m and $\Delta t = 0.001$ h. Parameter values used here are listed in Appendix A (Tables 2–3). Initial and boundary conditions are given by (17)–(23). In particular, as initial datum $\mathbf{X}(0)$, we set 90 cells equally distributed in the stripe $[600, 1180] \times [600, 640]$ (μm^2) at a distance between their centres of 17 μm, and then randomized around their position with radius in the range $[0, 3]$ (μm) and angles in $[0, 2\pi]$ (Figure 9 (a)). As initial condition $s(\mathbf{x}, 0)$ in equation (22) we fix $c_1 = 838$ μm (the inflection point of the hyperbolic tangent is about at the middle of the primordium), $c_2 = 200$ μm, and $[\bar{a}, \bar{b}] = [600, 5000]$ (μm). Then in (23) and (25) we choose $l = 20$ μm and $\varepsilon = 10$ μm.

Figures 9–11 show the numerical simulations of the lateral line evolution as described above at different time steps. As usual, green colour marks leader cells ($\varphi_i = 1$), and red colour the followers ($\varphi_i = 0$). Contour plot in the background is related to the FGF signal concentration, while 1D-plots refer to a longitudinal section in the graph of $s(\mathbf{x}, t)$, through the middle of the initial strip of chemoattractant. In our simulation we can observe, in the first few hours after migration starts, the leader-to-follower transition of some cells in the trailing region of the primordium, up to about $t = 6.5$ h when a first rosette starts detaching (Figure 9 (b)). This is consistent with the experimental results presented in the supplementary material in Nechiporuk and Raible (2008) and Lecaudey et al (2008), that show a time of about 3–6 h for the first rosette separation. Figure 10 (a) shows the formation of a second rosette in the new trailing region, meanwhile in the first rosette the lateral inhibition process is completed leaving two leader cells. Then in the next time steps, until about $t = 19$ h, we observe the detachment of the other two rosettes (Figures 10 (b), 11). We note that the somewhat rectangular shape of the rosettes is due to the initial position and to the large cell friction, and it should assume a more circular look on a larger time interval, because of the radial symmetry of the FGF sources.

In Figure 12 we have plotted migration velocity of the tip of the primordium versus time for 6 hours. Taking into account the velocity of 69 μm/h given in Lecaudey et al (2008), we observe a good agreement with our results. Moreover we observe a decrease in velocity in correspondence to the formation of the first rosette. This is substantially comparable with the velocity plot shown in Lecaudey et al (2008) in Figure 4 (c).

Another interesting behaviour of the migrating group of cells, that come out from our simulations, can be inferred considering the evolution in time of the SDF-1a stripe shown in the upper panels of Figures 9–11. Although we have considered a nonuniform initial distribution of chemoattractant like in (22), it appears somewhat constant, except an initial gradient along the primordium. During the motion, due to the contact degradation of the SDF-1a, the gradient of the chemoattractant becomes about zero along the trailing region of the primordium, while a new gradient is generated by the tip cells from the almost constant chemokine stripe. This feature of *self-generation* gradient has been recently showed on the zebrafish by Donà et al (2013). In the discussion of the parameters in Appendix A we will show that the total cell migration can be ensured even with an initial constant chemokine distribution along the x-axis.

Finally, from the numerical simulations, we observe a flocking behavior in cell migration, according to the results shown in Cucker and Smale (2007) and Ha and Liu (2009) for term (6), although in our model other effects are involved, as chemotaxis and adhesion-repulsion terms. We recall that in Ha and Liu (2009) flocking behaviour occurs unconditionally when the power of the denominator in (8) is less or equal to 1/2, and conditionally if this power is greater than 1/2. Taking into account our power in equation (8) and our initial data in (17) we would be in the case of conditional flocking if we used the

original Cucker-Smale model, and although we consider a truncated sensing domain and we have many additional effects, we observe consistent results.

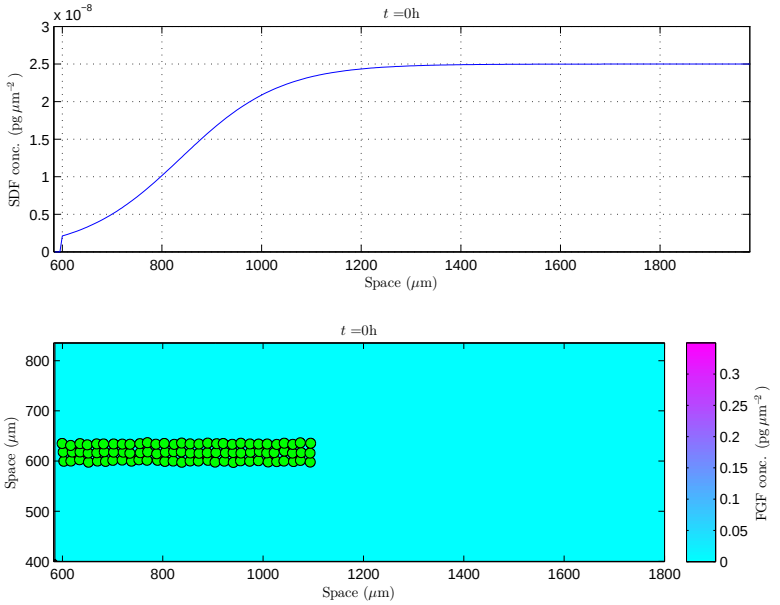

(a)

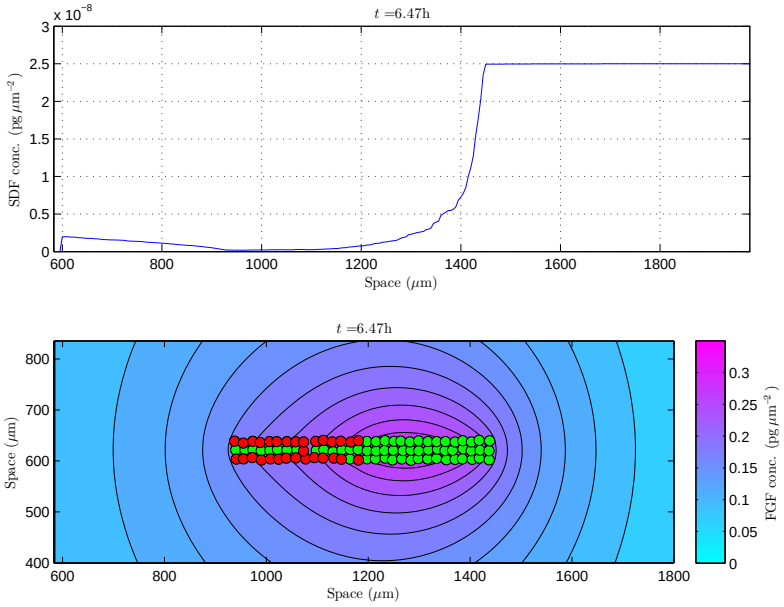

(b)

Fig. 9 Numerical simulation of the lateral line growth at five different time steps: $t = 0, 6.47$ h, next three time steps $t = 10.15, 15.64, 19$ h are plotted in Figures 10–11. System (26) is solved in the domain $\Omega = [0, 5000] \times [0, 1240]$ (μm^2) (plot shows only a part of the domain), with a spatial and temporal discretization given respectively by $\Delta x = \Delta y = 5\,\mu$m and $\Delta t = 0.001$ h. Parameter values used here are listed in Appendix A. Initial and boundary conditions are given by (17), (18), (19), and (21). In particular, about the initial condition $s(\mathbf{x}, 0)$, in equation (22) we have fixed $c_1 = 838$ μm, $c_2 = 200$ μm, and $[\bar{a}, \bar{b}] = [600, 5000]$ (μm). Then in (23) and (25) we have chosen $l = 20$ μm and $\varepsilon = 10$ μm. Green colour (●) is for leader cells, red colour (●) for the followers. The variable $s(\mathbf{x}, t)$ is shown in a 1D-plot, only along a longitudinal section through the middle of the initial strip of chemoattractant. Contour plot in the background indicates the FGF concentration.

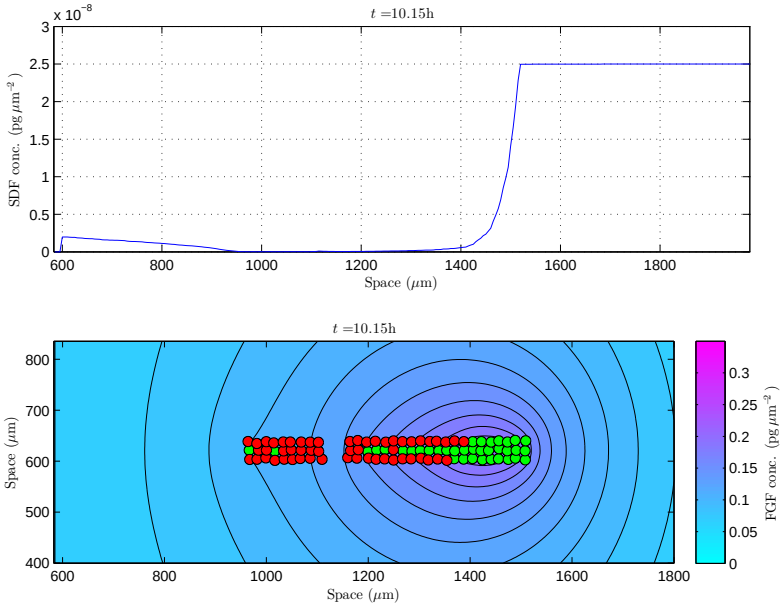

(a)

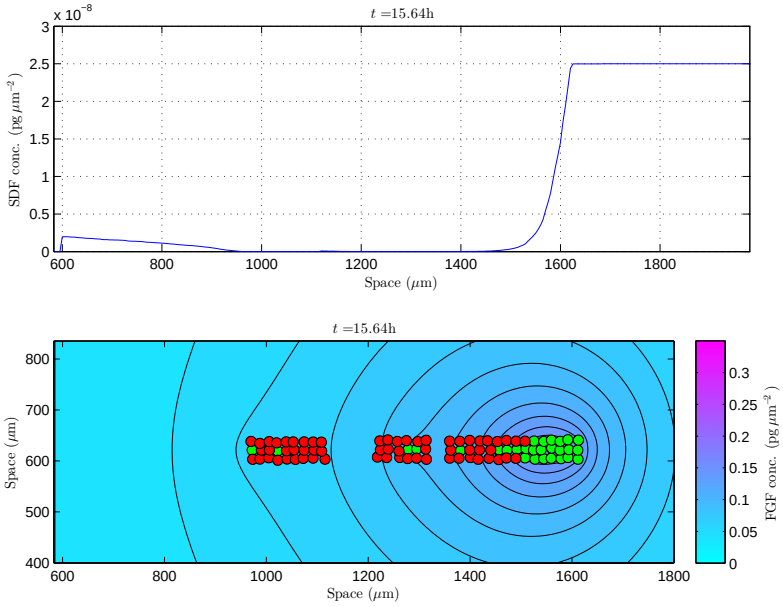

(b)

Fig. 10 Continuation of Figure 9. Numerical simulation of the lateral line growth at time steps: $t = 10.15, 15.64$ h.

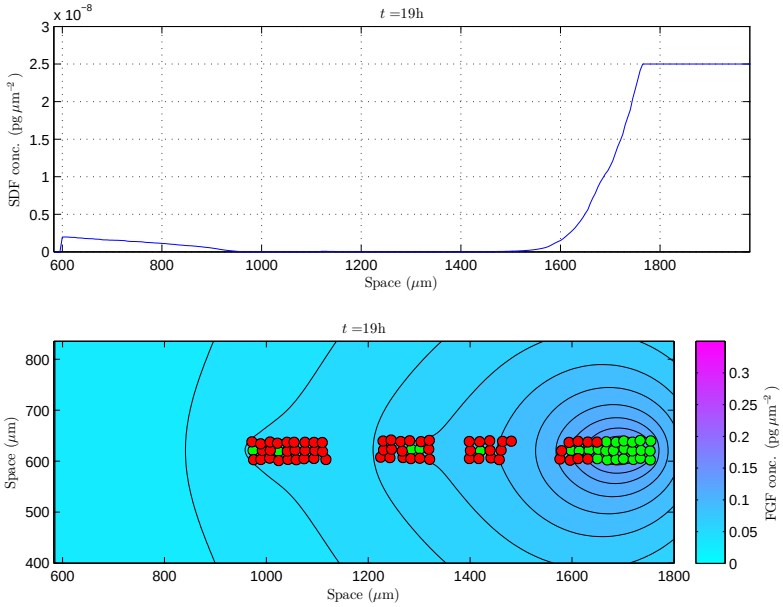

Fig. 11 Continuation of Figure 10. Numerical simulation of the lateral line growth at time step: $t = 19$ h.

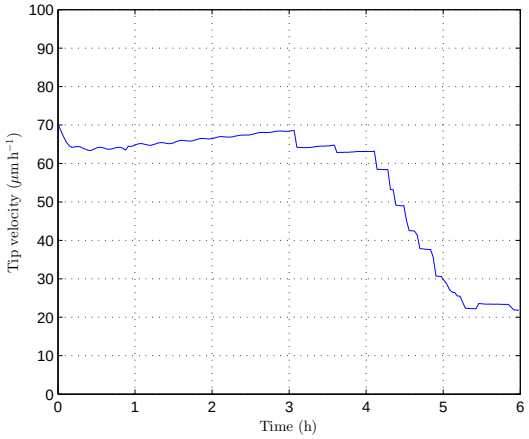

Fig. 12 Numerical dimensional plot of the velocity of tip of the primordium during migration versus time.

6 Conclusions

We have proposed in this paper a *discrete in continuous* mathematical model describing the formation of the lateral line in the zebrafish primordium. Under suitable hypotheses, we have shown that our model admits particular biologically relevant steady solutions. They corresponds to the formation of neuromasts along the two flanks of the embryo. Then their stability has been assessed numerically. Finally, the dynamical model has been tested by 2D numerical simulations and the results have been compared with some experimental observations. In particular we have observed that the moving cells can also self-generate their own chemokine gradient during the migration, a mechanism recently proved *in vivo* on the zebrafish by Donà et al (2013) (see also Appendix A).

Clearly we remark that the model proposed here presents some limits. Firstly, cells are supposed to be all equally circular, so that deformation effects are neglected. On the other hand they can be partially recovered introducing influence radii. Secondly, only a limited number of biological interactions have been modeled, and this in a time range starting with the beginning of the migration of the primordium. For example, biological phenomena occurring in the next few hours post-fertilization, or in the time after the rosettes deposition have not been taken into account. However we have followed the framework of the studies Nechiporuk and Raible (2008) and Lecaudey et al (2008), and a good concordance with the experimental data can be inferred.

Finally, we remark that with respect to these studies, some mechanism are biologically evident, as chemotaxis effects, cell adhesion-repulsion, damping effects, chemical signals diffusion, others, as our lateral inhibition term, cell alignment, change of parameters in the leader-follower transition, have been introduced to obtain a nice agreement with biological observations. It would be interesting to have experimental evidence in this regard.

A Parameter estimates

About the choice of the parameters of the model, we point out that while some values can be found or estimated from the biological or modelling literature, the others have been obtained by numerical data fitting or using some relations provided by the stationary model.

Tables 2–3 summarize respectively the values of the dimensional and nondimensional parameters. In the case of a range of variability for a parameter, the selected value, used in the simulations, is put in brackets. Finally, the last column in Table 2 specifies the references for the provided data.

Now we will make some comments in this regard. Firstly, cell radius R is fixed to 10 μm starting from the experimental data in Lecaudey et al (2008). Radii $\bar{R}$, R_1, are chosen to be equal to 20 μm, taking into account a possible effect of cell extensions. Radius R_2 is chosen to be equal to 20 μm considering the lateral inhibition activated when two cells start to be in touch. Radius R_3, concerning with the range of production or degradation of a chemical signaling, is set to be equal to R, because we think to a source or a drain defined by the dimension of a single cell. For R_4 and R_5 we fix respectively the values 20 μm and 25 μm. First value provides a repulsion force when two cells start to be overlapped (see equation $(10)_1$), second values implies an adhesion force in the spatial radial range 20–25 μm.

The values of Γ_0, α, β_{L}, β_{F}, γ, $\omega_{\mathrm{adh,F}}$, μ_{F}, δ/λ, and σ, are obtained by a numerical data fitting on the respective dimensionless values, in order to obtain in the simulations a cell migration velocity and a neuromasts formation consistent with the experimental results. This values are marked as "data fitting" in Table 2. In particular, Γ_0 controls the slope of the function (12), and its value has been chosen to mark a sharp difference in (12) between a cell in the centre of the primordium and one on the boundary. However, we have found that changes in the value of Γ_0 do not influence significantly the behaviour of the system. Then, by numerical tests we have seen that α, the coefficient related to the SDF-1a haptotactic effect, influences almost linearly the velocity of the cell migration in the first few hours before the transition leader-to-follower occurs (data not shown). This is expected from equation $(16)_1$ if we consider a regime of uniform velocity. The value for α is then fixed to have a cell velocity of ≈ 69 μm/h according to Lecaudey et al (2008). The values of β_{L} and β_{F} influence cell alignment. Without the alignment effect we have tested that the repulsion alone is not sufficient to ensure a distance between the cells consistent with the experimental observations. Values too small of β_{L} (about $< 5 \times 10^{17}$ h^{-1}) imply a large transverse compression of the primordium (with distances between the centres of the cells less than 40% of the cell diameter), causing even a crossing over of the cells (data not shown). The range of variability of β_{F}, $\omega_{\mathrm{adh,F}}$, μ_{F}, and γ, suggested in Table 2, have been taken in order to have the neuromasts detachment. Outside these ranges we can not reproduce a complete neuromasts formation. Precisely we find (data not shown) that, β_{F}, which is related to the alignment effect for follower cells is to be fixed, remaining in the range of β_{L}, at least two orders of magnitude smaller than β_{L} (see Table 2). Similarly, $\omega_{\mathrm{adh,F}}$, which represents the coefficient of the elastic adhesion for the followers, is to be chosen, in the range of $\omega_{\mathrm{adh,L}}$, about two orders of magnitude smaller than $\omega_{\mathrm{adh,L}}$. The parameter μ_{F}, that is the damping coefficient for a follower cell can be fixed about one order of magnitude larger than μ_{L}. Moreover for γ, the coefficient related to the FGF chemotactic effect, we find the range indicated in Table 2 (numerical data fitting not shown). The parameter δ/λ influences the switch variable $\varphi_i(t)$, and its increasing values produce, at the same time t, a number of leader-to-follower transition gradually decreasing (data not shown). The range proposed in Table 2 ensures, after about 10 h after the migration begins, a remaining number of leaders from 25% to about 55% over the total cell number in the primordium. These percentages are reasonable in view of the results presented in Lecaudey et al (2008), although it would be interesting to quantify, experimentally, the number of leader and follower cells. Finally, the parameter σ, related to the degradation of the SDF1-1a signal, affects the gradient of the chemoattractant and then the cell velocity during migration. Its value in Table 2 has been fixed to have, in the first few hours before leader-to-follower transition, a velocity consistent with the data in Lecaudey et al (2008). An interesting aspect, that has come out from our tests in Section 5, is that the cells of the primordium can self-generate their own gradient. Evidence for this has recently be obtained by Donà et al (2013). Even fixing a constant initial data for the SDF1-1a along the x-axis, with non zero values for σ we are able to reproduce the collective motion, though with a reduced velocity for the same values of σ. Comparing the case with initial gradient of SDF-1a and the case of zero initial gradient we find, for the value of σ used in Table 2, a decreased velocity of about 35% (data not shown). Anyway an initial gradient for the SDF-1a signal seems to be necessary, since for too large values of σ we observe a detachment of the head of the primordium.

About the information on the parameters arising from the stationary model, we refer to formulas (47), (48), (53), Table 1, and Figures 3–4. The first two relations give us a limitation for $k_{\mathrm{F}}^* := k_{\mathrm{F}}/\lambda$ and $k_{\mathrm{L}}^* := k_{\mathrm{L}}/\lambda$, the ratios of the coefficient of sensitivity to FGF signal and the coefficient of lateral inhibition for a leader and for a follower cell, while the third one provides a value of ω_{rep}, related to the repulsion coefficient, when we have fixed γ by a numerical data fitting, as mentioned before. Namely, the right hand side of these equations depend on N and d_1^* once the other parameters are chosen. So, to obtain the values in Tables 2–3 we have fixed for an example $N = 8$ and $d_1^* = 3/2R^*$. They represent reasonable values under the experimental observations in Nechiporuk and Raible (2008) and Lecaudey et al (2008).

Then a value for ξ, the parameter of FGF production, is obtained from the respective nondimensional value ξ^* in order to have the maximum nondimensional value of FGF $f_{\max}^* = 1$ in our domain. Finally, other constants are estimable from data available in literature:

$s_{\max}$, the maximum concentration of SDF-1a, from Kirkpatrick et al (2010); $f_{\max}$, the maximum concentration of FGF from Walshe and Mason (2003); $\omega_{\mathrm{adh,L}}$, the elastic adhesion for a leader cell, from Bell et al (1984); μ_{L}, the damping coefficient for a leader cell, from Rubinstein et al (2009); D, the diffusion coefficient of FGF, from Yeh et al (2003), Filion and Popel (2005) and a phenomenological formula in He and Niemeyer (2003); η, the degradation constant of FGF, from Beenken and Mohammadi (2009) and Lee and Blaber (2010), using the FGF half-life estimates.

Table 2: Estimates of physical parameter values.

Parameter	Definition	Value or range (used value)	Source
R	cell radius	10 μm	Lecaudey et al (2008)
$\bar{R}$	detection radius of chemicals	20 μm	biological assumption
R_1	detection radius of cellular alignment	20 μm	biological assumption
R_2	detection radius of lateral inhibition	20 μm	biological assumption
R_3	radius of production/degradation of chemicals	10 μm	biological assumption
R_4	radius of action of repulsion between cells	20 μm	biological assumption
R_5	radius of action of adhesion between cells	25 μm	biological assumption
T	characteristic time	1/3600 h	Rubinstein et al (2009)
$s_{\max}$	maximum concentration of SDF-1a	3.6×10^{-8}–6.5×10^{-8} (2.5×10^{-8}) pg μm^{-2}	Kirkpatrick et al (2010)
$f_{\max}$	maximum concentration of FGF	1×10^{-1}–(1.2×10^{-1}) pg μm^{-2}	Walshe and Mason (2003)
Γ_0	constant in function (12)	10 nondim.	data fitting
α	coefficient of SDF-1a haptotactic effect per unit mass	1.31×10^{27} μm^4 h^{-2} pg^{-1}	data fitting on Lecaudey et al (2008)
β_{L}	coefficient of cell flocking per unit mass for a leader cell	$>5\times10^{17}$ (5×10^{20}) h^{-1}	data fitting
β_{F}	coefficient of cell flocking per unit mass for a follower cell	5×10^{17} h^{-1}–$1.68\times10^{-2}\beta_{\mathrm{L}}$ (5×10^{18} h^{-1})	data fitting
γ	coefficient of FGF chemotactic effect per unit mass	1.08×10^{13}–(1.08×10^{20}) μm^4 h^{-2} pg^{-1}	data fitting
ω_{rep}	coefficient of repulsion per unit mass	2.03×10^{17} μm^2 h^{-2}	from steady model, formula (53)
$\omega_{\mathrm{adh,L}}$	elastic constant per unit mass for a leader cell	1.296×10^{14}–1.296×10^{19} (5.5×10^{16}) h^{-2}	Bell et al (1984)
$\omega_{\mathrm{adh,F}}$	elastic constant per unit mass for a follower cell	$0.55\times10^{-2}\omega_{\mathrm{adh,L}}$–$2\times10^{-2}\omega_{\mathrm{adh,L}}$ (5.5×10^{14} h^{-2})	data fitting
μ_{L}	damping coefficient for a leader cell per unit mass	(5.82×10^{14})–5.82×10^{15} h^{-1}	Rubinstein et al (2009)
μ_{F}	damping coefficient for a follower cell per unit mass	$8.42\,\mu_{\mathrm{L}}$–(5.82×10^{15} h^{-1})	data fitting
δ/λ	ratio of coefficient of sensitivity to SDF-1a and coefficient of lateral inhibition	8.8×10^{8}–1.36×10^{9} (1.12×10^{9}) pg^{-1} μm^2	data fitting

k_L/λ	ratio of coefficient of sensitivity to FGF signal for a leader cell and coefficient of lateral inhibition	< 1.8187 (1.7) nondim.	from steady model, formula (48)
k_F/λ	ratio of coefficient of sensitivity to FGF signal for a follower cell and coefficient of lateral inhibition	≥ 1.1619 (17) nondim.	from steady model, formula (47)
D	diffusion coefficient	69985–84184 (78950) $\mu m^2\,s^{-1}$	He and Niemeyer (2003); Filion and Popel (2005); Yeh et al (2003)
ξ	coefficient of production of FGF	2.9592 $pg\,\mu m^{-2}\,h^{-1}$	data fitting on Walshe and Mason (2003)
η	degradation constant of FGF	0.09–0.69(0.2) h^{-1}	Beenken and Mohammadi (2009); Lee and Blaber (2010)
σ	degradation constant of SDF-1a	0.55–0.7(0.6) h^{-1}	data fitting on Lecaudey et al (2008)

Table 3: Estimates of dimensionless parameter values.

Parameter	Definition	Value or range (used value)
$\bar{R}^*$	$\bar{R}/R$	2
R_1^*	R_1/R	2
R_2^*	R_2/R	2
R_3^*	R_3/R	1
R_4^*	R_4/R	2
R_5^*	R_5/R	2,5
Γ_0	Γ_0	10
α^*	$\alpha s_{max} T^2/R^2$	2.53×10^{10}
β_L^*	$\beta_L T$	$> 1.39 \times 10^{14}$ (1.39×10^{17})
β_F^*	$\beta_F T$	1.39×10^{14}–$1.68 \times 10^{-2}\beta_L^*$ (1.39×10^{15})
γ^*	$\gamma f_{max} T^2/R^2$	10^3–(10^{10})
ω_{rep}^*	$\omega_{rep} T^2/R^2$	1.57×10^8
$\omega_{adh,L}^*$	$\omega_{adh,L} T^2$	10^7–10^{12} (4.24×10^9)
$\omega_{adh,F}^*$	$\omega_{adh,F} T^2$	$0.55\times10^{-2}\omega_{adh,L}^*$ –$2\times10^{-2}\omega_{adh,L}^*$ (4.24×10^7)

μ_{L}^*	$\mu_{\mathrm{L}}T$	(1.62×10^{11})–1.62×10^{12}
μ_{F}^*	$\mu_{\mathrm{F}}T$	$8.42\mu_{\mathrm{L}}^*$–(1.62×10^{12})
δ^*	$\delta s_{\max}/\lambda$	22–34 (28)
k_{L}^*	k_{L}/λ	<1.8187 (1.7)
k_{F}^*	k_{F}/λ	≥ 1.1619 (17)
D^*	DT/R^2	0.1944–0.2338 (0.2193)
ξ^*	$\xi T/f_{\max}$	0.0069
η^*	ηT	2.5×10^{-5}–1.92×10^{-4} (5.56×10^{-5})
σ^*	σT	1.531×10^{-4}–1.948×10^{-4} (1.67×10^{-4})

B Numerical approximation

In this appendix we discuss the numerical approximation scheme employed for system (26) in the numerical simulations.

The methods used in the numerical simulations employ a 2D finite difference scheme. We consider the spatial domain $\Omega=[a,b]\times[c,d]$ and the spatial steps Δx, Δy, such that $[a,b]$ is divided in $M=\frac{b-a}{\Delta x}$ intervals, and $[c,d]$ in $N=\frac{d-c}{\Delta y}$ intervals, with M, N integers. Then we introduce a Cartesian grid consisting of grid points (x_m,y_n), where $x_m=m\Delta x$ and $y_n=n\Delta y$. The same can be done for the time interval $[0,T]$, in this case if Δt is the time step, t_k will be the n-th temporal step, i.e. $t_k=k\Delta t$. With the notation $u_{m,n}^k$ we denote the approximation of a function $u(x,y,t)$ at the grid point (x_m,y_n,t_k).

~~Now, we start to describe~~ the approximation of the parabolic equation $(26)_3$. ~~The right hand side is made by~~ the diffusion term, the source term, and the stiff degradation term $-\eta^* f$. In order to eliminate this last quantity we perform the classical exponential transformation

$$f(\mathbf{x},t)=e^{-\eta^* t}u(\mathbf{x},t), \tag{61}$$

which leads to the diffusion equation with source for $u(\mathbf{x},t)$:

$$\partial_t u=D^*\Delta u+e^{\eta^* t}\xi^*\sum_{j=1}^{N_{\mathrm{tot}}}\varphi_j\chi_{\mathbf{B}(\mathbf{X}_j,R_3^*)}, \tag{62}$$

with initial and boundary conditions

$$u(\mathbf{x},0)=0;\quad \frac{\partial u}{\partial \mathbf{n}}=0,\quad \text{on } \partial\Omega, \tag{63}$$

given by (19). For this equation we apply a central difference scheme in space, i.e. the 5-point stencil for the Laplacian, and the parabolic Crank-Nicolson scheme in time. The source term in taken in explicit, in the form

$$\xi^*\sum_{j=1}^{N_{\mathrm{tot}}}\varphi_j^k\chi_{\mathbf{B}(\mathbf{X}_j^k,R_3^*)},$$

where the discretized characteristic function is

$$\chi_{\mathbf{B}(\mathbf{X}_j^k,R_3^*)} = \begin{cases} 1, \text{ if } (x_m,y_n) \in \mathbf{B}(\mathbf{X}_j^k,R_3^*); \\ 0, \quad \text{otherwise.} \end{cases} \tag{64}$$

The numerical scheme can be written as

$$\begin{aligned} \frac{u_{m,n}^{k+1}-u_{m,n}^k}{\Delta t} &= \frac{D^*}{2}\left(D_x^2u^{k+1}+D_y^2u^{k+1}\right)+\frac{D^*}{2}\left(D_x^2u^k+D_y^2u^k\right) \\ &+\frac{1}{2}e^{\eta^*(k+1)\Delta t}\xi^*\sum_{j=1}^{N_{\text{tot}}}\varphi_j^k\chi_{\mathbf{B}(\mathbf{X}_j^k,R_3^*)} \\ &+\frac{1}{2}e^{\eta^* k\Delta t}\xi^*\sum_{j=1}^{N_{\text{tot}}}\varphi_j^k\chi_{\mathbf{B}(\mathbf{X}_j^k,R_3^*)}, \end{aligned}$$

where the second finite differences D_x^2u and D_y^2u are given by

$$\begin{aligned} D_x^2u^k &:= \frac{u_{m-1,n}^k-2u_{m,n}^k+u_{m+1,n}^k}{\Delta x^2}, \\ D_y^2u^k &:= \frac{u_{m,n-1}^k-2u_{m,n}^k+u_{m,n+1}^k}{\Delta y^2}. \end{aligned} \tag{65}$$

For Neumann boundary condition (63) we use a second order accurate onesided approximation, namely:

$$\begin{aligned} \frac{\partial u^k}{\partial x}(x_0,y_n) &\approx \frac{1}{2\Delta x}\left(-3u_{0,n}^k+4u_{1,n}^k-u_{2,n}^k\right)=0, && n=1,\dots,N-1, \\ \frac{\partial u^k}{\partial x}(x_M,y_n) &\approx \frac{1}{2\Delta x}\left(3u_{M,n}^k-4u_{M-1,n}^k+u_{M-2,n}^k\right)=0, && n=1,\dots,N-1, \\ \frac{\partial u^k}{\partial y}(x_m,y_0) &\approx \frac{1}{2\Delta y}\left(-3u_{m,0}^k+4u_{m,1}^k-u_{m,2}^k\right)=0, && m=1,\dots,M-1, \\ \frac{\partial u^k}{\partial x}(x_m,y_N) &\approx \frac{1}{2\Delta y}\left(3u_{m,N}^k-4u_{m,N-1}^k+u_{m,N-2}^k\right)=0, && m=1,\dots,M-1. \end{aligned} \tag{66}$$

In relation to the stationary form of $(26)_3$

$$D^*\Delta f = \eta^* f - \xi^*\chi_{\mathbf{B}(\mathbf{X}_{\text{L}},R_3^*)}, \tag{67}$$

$$\frac{\partial f}{\partial \mathbf{n}} = 0, \quad \text{on } \partial\Omega, \tag{68}$$

used in Section 4 (eqs. (45)–(46)) to discuss the steady states of the model, we adopt the central scheme:

$$D^*\left(D_x^2f+D_y^2f\right) = \eta^* f_{m,n} - \xi^*\chi_{\mathbf{B}(\mathbf{X}_{\text{L}},R_3^*)}, \tag{69}$$

in which D_x^2u and D_y^2u are defined by (65) and $\chi_{\mathbf{B}(\mathbf{X}_{\text{L}},R_3^*)}$ is given by (64), where here $\mathbf{X}_{\text{L}}$ is the fixed centre of the leader cell, the only one that produces FGF signal. Then boundary condition (68) is treated using (66) for $f_{m,n}$.

For equation $(26)_4$ we put the right hand side in explicit, and we write the numerical scheme

$$\frac{s_{m,n}^{k+1}-s_{m,n}^k}{\Delta t} = -\sigma^* s_{m,n}^k\sum_{j=1}^{N_{\text{tot}}}\chi_{\mathbf{B}(\mathbf{X}_j^k,R_3^*)}, \tag{70}$$

where the characteristic function is computed as in (64).

~~Now we consider~~ equation $(26)_1$, ~~that is reduce~~ to a first order system in the form (60). For $(60)_1$ we apply a one step IMEX method, putting totally implicit in time the term containing $\mathbf{H}\left(\mathbf{Y}_j - \mathbf{Y}_i\right)$ and the term $-\left[\mu_{\mathrm{F}}^* + (\mu_{\mathrm{L}}^* - \mu_{\mathrm{F}}^*)\varphi_i\right]\mathbf{Y}_i$ at the right hand side, while totally explicit the other ~~addends~~ (Hundsdorfer and Verwer, 2003). The two-dimensional integrals in $(60)_1$ can be computed by a 2D quadrature formula, which due to the truncated Gaussian weight function $w_i(\mathbf{x})$ given in (4), is reduced to a sum of the discretized integrand function on the grid points belonging to the ball $\mathbf{B}(\mathbf{X}_i, \bar{R}^*)$. For a integrand function $g(\mathbf{x}, t)$ holds

$$\int_{\mathbf{B}(\mathbf{X}_i, \bar{R}^*)} g(\mathbf{x}, t) w_i(\mathbf{x})\, d\mathbf{x} \approx \sum_{m,n \text{ s.t. } (x_m, y_n) \in \mathbf{B}(\mathbf{X}_i^k, \bar{R}^*)} g_{m,n}^k (w_i)_{m,n}^{(k)}, \tag{71}$$

where $(w_i)^{(k)}$ is the weight function centred in $\mathbf{X}^k$, at time step t_k. The same holds for the quantity W defined in (5), which is approximated by

$$\mathcal{W} := \sum_{m,n \text{ s.t. } (x_m, y_n) \in \mathbf{B}(\mathbf{X}_i^k, \bar{R}^*)} (w_i)_{m,n}^{(k)}. \tag{72}$$

The gradients in equation $(60)_1$ are approximated with the first order difference:

$$\nabla g(x_m, y_n, t_k) \approx \nabla_{m,n} g^k, \tag{73}$$

where

$$\nabla_{m,n} g^k := \left(\frac{g_{m+1,n}^k - g_{m,n}^k}{\Delta x}, \frac{g_{m,n+1}^k - g_{m,n}^k}{\Delta y} \right). \tag{74}$$

Equation $(60)_2$ is then solved with the forward Euler method. The numerical scheme for equations $(60)_{1,2}$ can be summarized as

$$\begin{cases} \dfrac{\mathbf{Y}_i^{k+1} - \mathbf{Y}_i^k}{\Delta t} = \dfrac{\alpha^*}{\mathcal{W}} \displaystyle\sum_{m,n \text{ s.t. } (x_m, y_n) \in \mathbf{B}(\mathbf{X}_i^k, \bar{R}^*)} \left(\nabla_{m,n} s^k\right) (w_i)_{m,n}^{(k)} \\ \qquad + \dfrac{\gamma^*(1 - \varphi_i^k)}{\mathcal{W}} \displaystyle\sum_{m,n \text{ s.t. } (x_m, y_n) \in \mathbf{B}(\mathbf{X}_i^k, \bar{R}^*)} \left(\nabla_{m,n} f^k\right) (w_i)_{m,n}^{(k)} \\ \qquad + \dfrac{1}{\bar{N}_i} \displaystyle\sum_{j : \mathbf{X}_j^k \in \mathbf{B}(\mathbf{X}_i^k, R_1^*) \setminus \{\mathbf{X}_i^k\}} \mathbf{H}(\mathbf{Y}_j^{k+1} - \mathbf{Y}_i^{k+1}) \\ \qquad + \displaystyle\sum_{j : \mathbf{X}_j^k \in \mathbf{B}(\mathbf{X}_i^k, R_5^*) \setminus \{\mathbf{X}_i^k\}} \mathbf{K}(\mathbf{X}_j^k - \mathbf{X}_i^k) - \left[\mu_{\mathrm{F}}^* + (\mu_{\mathrm{L}}^* - \mu_{\mathrm{F}}^*)\varphi_i\right] \mathbf{Y}_i^{k+1}, \\ \dfrac{\mathbf{X}_i^{k+1} - \mathbf{X}_i^k}{\Delta t} = \mathbf{Y}_i^k, \end{cases}$$

in which

$$\bar{N}_i := \mathrm{card}\left\{ j : \mathbf{X}_j^k \in \mathbf{B}(\mathbf{X}_i^k, R_1^*) \right\},$$

$$\mathbf{H}\left(\mathbf{Y}_j^k - \mathbf{Y}_i^k\right) := \left[\beta_{\mathrm{F}}^* + (\beta_{\mathrm{L}}^* - \beta_{\mathrm{F}}^*)\varphi_i^k \varphi_j^k\right] \frac{R_1^{*2}}{R_1^{*2} + ||\mathbf{X}_j^k - \mathbf{X}_i^k||^2} (\mathbf{Y}_j^k - \mathbf{Y}_i^k),$$

and

$$\mathbf{K}(\mathbf{X}_j^k - \mathbf{X}_i^k) := \begin{cases} -\omega_{\text{rep}}^* \left(\dfrac{1}{||\mathbf{X}_j^k - \mathbf{X}_i^k||} - \dfrac{1}{R_4^*} \right) \dfrac{\mathbf{X}_j^k - \mathbf{X}_i^k}{||\mathbf{X}_j^k - \mathbf{X}_i^k||}, & \text{if } ||\mathbf{X}_j^k - \mathbf{X}_i^k|| \leq R_4^*; \\ \bar{\omega}_{\text{adh}}^* \left(||\mathbf{X}_j^k - \mathbf{X}_i^k|| - R_4^* \right) \dfrac{\mathbf{X}_j^k - \mathbf{X}_i^k}{||\mathbf{X}_j^k - \mathbf{X}_i^k||}, & \text{if } R_4^* < ||\mathbf{X}_j^k - \mathbf{X}_i^k|| \leq R_5^*; \end{cases}$$

with

$$\bar{\omega}_{\text{adh}}^* := \omega_{\text{adh,F}}^* + (\omega_{\text{adh,L}}^* - \omega_{\text{adh,F}}^*)\varphi_i^k \varphi_j^k.$$

Finally variable $\varphi_i(t)$ is computed putting in explicit the right hand side of $(26)_2$ and using the above discretizations:

$$\varphi_i^{k+1} = \begin{cases} 0, \text{ if } \dfrac{\delta^*}{\mathcal{W}} \displaystyle\sum_{m,n \text{ s.t. } (x_m,y_n) \in \mathbf{B}(\mathbf{X}_i^k, \bar{R}^*)} s_{m,n}^k (w_i)_{m,n}^{(k)} \\ \quad - \dfrac{k_{\text{F}}^* + (k_{\text{L}}^* - k_{\text{F}}^*)\varphi_i^k}{\mathcal{W}} \displaystyle\sum_{m,n \text{ s.t. } (x_m,y_n) \in \mathbf{B}(\mathbf{X}_i^k, \bar{R}^*)} \dfrac{f_{m,n}^k}{1 + f_{m,n}^k} (w_i)_{m,n}^{(k)} \\ \quad + \Gamma(n_i^{(k)}) \leq 0, \\ 1, \quad \text{otherwise}, \end{cases}$$

where $n_i^{(k)}$ is given by (28) at k-th time step, that is

$$n_i^{(k)} := \text{card} \left\{ j : \mathbf{X}_j^k \in \mathring{\mathbf{B}}(\mathbf{X}_i^k, R_2^*) \backslash \left\{ \mathbf{X}_i^k \right\} \right\}.$$

About the spatial and temporal step, in the numerical simulations we chose $\Delta x = \Delta y$ and, since for short time the value of variable $u(\mathbf{x}, t)$ in (62) is near to zero and the forcing term is discontinuous, we need to stabilize the numerical scheme for few time steps using the standard parabolic CFL condition $\Delta t \sim \frac{\Delta x^2}{D^*}$. In practice, after the first time steps, we were able to change the CFL condition and to adopt the more favorable restriction $\Delta t \sim \Delta x$.

Acknowledgements We thank Andrea Tosin for some useful discussions and suggestions. The research leading to these results has received funding from the European Union Seventh Framework Programme [FP7/2007-2013] under grant agreement n. 257462 HYCON2 Network of excellence. This work has also been partially supported by the PRIN project 2008-2009 "Equazioni iperboliche non lineari e fluidodinamica". The authors Ezio Di Costanzo and Luigi Preziosi are members of the Gruppo Nazionale per la Fisica Matematica (GNFM), Roberto Natalini is member of the Gruppo Nazionale per l'Analisi Matematica, la Probabilità e le loro Applicazioni (GNAMPA) of the Istituto Nazionale di Alta Matematica (INdAM).

References

Albi G, Pareschi L (2013) Modeling self-organized systems interacting with few individuals: From microscopic to macroscopic dynamics. Appl Math Lett 26(4):397–401

Arboleda-Estudillo Y, Krieg M, Stühmer J, Licata NA, Muller DJ, Heisenberg CP (2010) Movement Directionality in Collective Migration of Germ Layer Progenitors. Curr Biology 20:161–169

Bayly PV, Taber LA, Carlsson AE (2012) Damped and persistent oscillations in a simple model of cell crawling. J R Soc Interface 9(71):1241–1253

Beenken A, Mohammadi M (2009) The fgf family: biology, pathophysiology and therapy. Nat Rev Drug Discov 8(3):235–253

Bell GI, Dembo M, Bongrand P (1984) Cell adhesion. Competition between nonspecific repulsion and specific bonding. Biophys J 45(6):1051–1064

Böttcher RT, Niehrs C (2005) Fibroblast Growth Factor Signaling during Early Vertebrate Development. Endocr Rev 26(1):63–77

Chitnis AB, Nogare DD, Matsuda M (2012) Building the Posterior Lateral Line System in Zebrafish. Dev Neurobiol 72(3):234–255

Colombi A, Scianna M, Tosin A (2011) Differentiated cell behavior: a multiscale approach using measure theory. submitted, URL `http://arxiv.org/abs/1108.1212v2`

Coombs S, Netten SV (2005) The Hydrodynamics and Structural Mechanics of the Lateral Line System. Fish Physiology 23:103–139

Cristiani E, Piccoli B, Tosin A (2011) Multiscale modeling of granular flows with application to crowd dynamics. Multiscale Model Sim 9(1):155–182

Cucker F, Smale S (2007) Emergent Behavior in Flocks. Ieee T Automat Contr 52(5):852–862

Donà E, Barry JD, Valentin G, Quirin C, Khmelinskii A, Kunze A, Durdu S, Newton LR, Fernandez-Minan A, Huber W, Knop M, Gilmour D (2013) Directional tissue migration through a self-generated chemokine gradient. Nature 503:285–289

D'Orsogna MR, Chuang YL, Bertozzi AL, Chayes LS (2006) Self-Propelled Particles with Soft-Core Interactions: Patterns, Stability, and Collapse. Phys Rev Lett 96(10):104302

Draper BW, Morcos PA, Kimmel CB (2001) Inhibition of Zebrafish fgf8 Pre-mRNA Splicing With Morpholino Oligos: A Quantifiable Method for Gene Knockdown. Genesis 30:154–156

Eisenbach M, Lengeler JW (2004) Chemotaxis. Imperial College Press

Filion RJ, Popel AS (2005) Intracoronary administration of FGF-2: a computational model of myocardial deposition and retention. Am J Physiol Heart Circ Physiol 288(1):H263–H279

Fournier MF, Sauser R, Ambrosi D, Meister JJ, Verkhovsky AB (2010) Force transmission in migrating cells. J Cell Biol 188(2):287–297

Ghysen A, Chaudière CD (2004) Development of the zebrafish lateral line. Curr Opin Neurobiol 14:67–73

Ha SY, Liu JG (2009) A simple proof of the Cucker-Smale flocking dynamics and mean-field limit. Commun Math Sci 7(2):297–325

Haas P, Gilmour D (2006) Chemokine Signaling Mediates Self-Organizing Tissue Migration in the Zebrafish Lateral Line. Dev Cell 10:673–680

Haddon C, Smithers L, Schneider-Maunoury S, Coche T, Henrique D, Lewis J (1998) Multiple delta genes and lateral inhibition in zebrafish primary neurogenesis. Development 125:359–370

Hart A, Papadopoulou S, Edlund H (2003) Fgf10 Maintains Notch Activation, Stimulates Proliferation, and Blocks Differentiation of Pancreatic Epithelial Cells. Dev Dynam 228:185–193

He L, Niemeyer B (2003) A Novel Correlation for Protein Diffusion Coefficients Based on Molecular Weight and Radius of Gyration. Biotechnol Prog 19:544–548

Hundsdorfer W, Verwer JG (2003) Numerical Solution of Time-Dependent Advection-Diffusion-Reaction Equations. Computational Mathematics, Springer

Itoh M, Chitnis AB (2001) Expression of proneural and neurogenic genes in the zebrafish lateral line primordium correlates with selection of hair cell fate in neuromasts. Mech

Develop 102:263–266
Joie J, Lei Y, Colin T, Durrieu MC, Poignard C, Saut O (2013) Modelling of migration and orientation of endothelial cells on micropatterned polymers, URL `http://hal.inria.fr/docs/00/99/07/77/PDF/RR-discret2.pdf`, research report INRIA RR-8252, 20 pp
Kerstetter A, Azodi E, Marrs JA, Liu Q (2004) Cadherin-2 Function in the Cranial Ganglia and Lateral Line System of Developing Zebrafish. Dev Dynam 230:137–143
Kirkpatrick B, Nguyen L, Kondrikova G, Herberg S, Hill WD (2010) Brief Technical Note: Stability of Human Stromal-Derived Factor-1α (CXCL12α) After Blood Sampling. Ann Clin Lab Sci 40(3):257–260
Lecaudey V, Akdogan GC, Norton WHJ, Gilmour D (2008) Dynamic fgf signaling couples morphogenesis and migration in the zebrafish lateral line primordium. Development 135:2695–2705, DOI 10.1242/dev.025981
Lee J, Blaber M (2010) Increased Functional Half-life of Fibroblast Growth Factor-1 by Recovering a Vestigial Disulfide Bond. Journal Of Proteins And Proteomics 1(2):37–42
Li Q, Shirabe K, Kuwada JY (2004) Chemokine signaling regulates sensory cell migration in zebrafish. Dev Biol 269:123–136
Liu Q, Ensign RD, Azodi E (2003) Cadherin-1, -2 and -4 expression in the cranial ganglia and lateral line system of developing zebrafish. Gene Expr Patterns 3:653–658
Liu Q, Dalman MR, Sarmah S, Chen S, Chen Y, Hurlbut AK, Spencer MA, L P, Marrs JA (2011) Cell Adhesion Molecule Cadherin-6 Function in Zebrafish Cranial and Lateral Line Ganglia Development. Dev Dynam 240:1716–1726
Matsuda M, Chitnis AB (2010) Atoh1a expression must be restricted by Notch signaling for effective morphogenesis of the posterior lateral line primordium in zebrafish. Development 137:3477–3487
Mertz AF, Che Y, Banerjee S, Goldstein J, Rosowski KR, Revilla SF, Niessen CM, Marchetti MC, Dufresne ER, Horsley V (2013) Cadherin-Based Intercellular Adhesions Organize Epithelial Cell-Matrix Traction Forces. P Natl Acad Sci USA 103(3):842–847
Mizoguchi T, Togawa S, Kawakami K, Itoh M (2011) Neuron and Sensory Epithelial Cell Fate Is Sequentially Determined by Notch Signaling in Zebrafish Lateral Line Development. J Neurosci 31(43):15,522–15,530
Murray JD (2003) Mathematical biology II: Spatial Models and Biomedical Applications. Third edition. Springer
Nechiporuk A, Raible D (2008) FGF-Dependent Mechanosensory Organ Patterning in Zebrafish. Science 320:1774–1777
Papusheva E, Heisenberg CP (2010) Spatial organization of adhesion: force-dependent regulation and function in tissue morphogenesis. EMBO J 29:2753–2768
Perthame B (2007) Transport equations in biology. Birkhäuser
Rubinstein B, Fournier MF, Jacobson K, Verkhovsky AB, Mogilner A (2009) Actin-Myosin Viscoelastic Flow in the Keratocyte Lamellipod. Biophys J 97:1853–1863
Sarrazin AF, Nuñez VA, Sapède D, Tassin V, Chaudière CD, A G (2010) Origin and Early Development of the Posterior Lateral Line System of Zebrafish. J Neurosci 30(24):8234–8244
Sepúlveda N, Petitjean L, Cochet O, Grasland-Mongrain E, Silberzan P, Hakim V (2013) Collective Cell Motion in an Epithelial Sheet Can Be Quantitatively Described by a Stochastic Interacting Particle Model. PLOS Computational Biology 9(3):e1002944
Streichan SJ, Velentin G, Gilmour D, Hufnagel L (2011) Collective cell migration guided by dynamically maintained gradients. Phys Biol 8:045004
Sweet EM, Vemaraju S, Riley BB (2011) Sox2 and Fgf interact with atoh1 to promote sensory competence throughout the zebrafish inner ear. Dev Biol 358:113–121
Szabò B, Szöllösi GJ, Gönci B, Jurànyi Z, Selmeczi D, Vicsek T (2006) Phase transition in the collective migration of tissue cells: Experiment and model. Phys Rev E 74(6):061908
Vicsek T, Cziròk A, Ben-Jacob E, Cohen I, Shochet O (1995) Novel Type of Phase Transition in a System of Self-Driven Particles. Phys Rev Lett 75(6):1226–1229
Walshe J, Mason I (2003) Fgf signalling is required for formation of cartilage in the head. Dev Biol 264:522–536
Yeh BK, Igarashi M, Eliseenkova AV, Plotnikov AN, Sher I, Ron D, Aaronson SA, Mohammadi M (2003) Structural basis by which alternative splicing confers specificity in

fibroblast growth factor receptors. P Natl Acad Sci USA 100(5):2266–2271